

## A CONNECTION BETWEEN OBSCURATION AND STAR FORMATION IN LUMINOUS QUASARS

CHIEN-TING J. CHEN<sup>1</sup>, RYAN C. HICKOX<sup>1</sup>, STACEY ALBERTS<sup>2</sup>, CHRIS M. HARRISON<sup>3</sup>, DAVID M. ALEXANDER<sup>3</sup>, ROBERTO ASSEF<sup>4</sup>, MARK BRODWIN<sup>5</sup>, MICHAEL J. I. BROWN<sup>6</sup>, AGNESE DEL MORO<sup>3</sup>, WILLIAM R. FORMAN<sup>7</sup>, VAROUJAN GORJIAN<sup>8</sup>, ANDREW D. GOULDING<sup>7</sup>, KEVIN N. HAINLINE<sup>1</sup>, CHRISTINE JONES<sup>7</sup>, CHRISTOPHER S. KOCHANEK<sup>9</sup>, STEPHEN S. MURRAY<sup>10</sup>, ALEXANDRA POPE<sup>2</sup>, EMMANOUEL ROVILOS<sup>3</sup>, AND DANIEL STERN<sup>8</sup>

<sup>1</sup> Department of Physics and Astronomy, Dartmouth College, 6127 Wilder Laboratory, Hanover, NH 03755, USA; ctchen@dartmouth.edu

<sup>2</sup> Department of Physics, Amherst, University of Massachusetts, Amherst, MA 01003, USA

<sup>3</sup> Department of Physics, Durham University, South Road, Durham, DH1 3LE, UK

<sup>4</sup> Núcleo de Astronomía de la Facultad de Ingeniería, Universidad Diego Portales, Avenida Ejército Libertador 441, Santiago, Chile

<sup>5</sup> University of Missouri, 5110 Rockhill Road, Kansas City, MO 64110, USA

<sup>6</sup> School of Physics, Monash University, Clayton 3800, Victoria, Australia

<sup>7</sup> Harvard-Smithsonian Center for Astrophysics, 60 Garden Street, Cambridge, MA 02138, USA

<sup>8</sup> Jet Propulsion Laboratory, California Institute of Technology, 4800 Oak Grove Drive, Pasadena, CA 91109, USA

<sup>9</sup> Department of Astronomy, Ohio State University, 140 West 18th Avenue, Columbus, OH 43210, USA

<sup>10</sup> Department of Physics and Astronomy, The Johns Hopkins University, 3400 N. Charles Street, Baltimore, MD 21218, USA

Received 2014 August 21; accepted 2015 January 20; published 2015 March 20

## ABSTRACT

We present a measurement of the star formation properties of a uniform sample of mid-IR-selected, optically unobscured, and obscured quasars (QSO1s and QSO2s) in the Boötes survey region. We use a spectral energy distribution analysis for photometric data spanning optical to far-IR wavelengths to separate the active galactic nucleus (AGN) and host galaxy components. We find that when compared to a matched sample of QSO1s, the QSO2s have roughly twice the far-IR detection fractions, far-IR fluxes, and infrared star formation luminosities ( $L_{\text{IR}}^{\text{SF}}$ ). Correspondingly, we show that the AGN obscured fraction rises from 0.3 to 0.7 between  $(4\text{--}40) \times 10^{11} L_{\odot}$ . We also find evidence associating X-ray absorption with the presence of far-IR-emitting dust. Overall, these results are consistent with galaxy evolution models in which quasar obscuration is associated with dust-enshrouded starburst galaxies.

*Key words:* galaxies: active – galaxies: starburst – infrared: galaxies – quasars: general – X-rays: galaxies

## 1. INTRODUCTION

Quasars, the most luminous active galactic nuclei (AGNs)<sup>11</sup>, have been linked to galaxies with active star formation (SF) ever since the discovery of their observational connection to ultraluminous infrared galaxies (ULIRGs, galaxies more luminous than  $10^{12} L_{\odot}$ , e.g., Sanders et al. 1988). One well-studied scenario for massive galaxy evolution posits that gas-rich galaxy major mergers trigger both rapid supermassive black hole (SMBH) accretion and intense SF. This scenario associates the dust-enshrouded starburst with strong nuclear obscuration that is later expelled by the powerful AGN, implying an evolutionary link between unobscured (type 1) and obscured (type 2) quasars (e.g., Di Matteo et al. 2005; Hopkins et al. 2006; Gilli et al. 2007; Somerville et al. 2008; Treister et al. 2009).

On the other hand, the “unification model” of AGN ascribes obscuration of AGNs to different lines of sight through a dusty “torus” surrounding the SMBH (e.g., Urry & Padovani 1995; Antonucci 1993). This model predicts no difference in host galaxy properties between obscured and unobscured AGNs. To date, it is still a matter of debate whether the obscuration in luminous quasars can be explained solely by the orientation-based unification model or if it is also enhanced due to dust on larger scales throughout the host galaxy. Several studies have shown results supporting a scenario departing from the unification model, such as the enhanced SF activity (e.g.,

Canalizo & Stockton 2001; Page et al. 2004; Hiner et al. 2009; Brusa et al. 2008; Shan & Chen 2012) and the more disturbed structure (e.g., Lacy et al. 2007b) of the host galaxies of dust-obscured quasars when compared to unobscured quasars. Clustering of different types of AGNs have also shown that obscured AGNs are more strongly clustered than unobscured AGNs (e.g., Hickox et al. 2011; Donoso et al. 2014; DiPompeo et al. 2014). However, other studies have found no significant difference between obscured and unobscured AGN populations in their morphological and SF properties (e.g., Sturm et al. 2006; Zakamska et al. 2006, 2008; Mainieri et al. 2011; Schawinski et al. 2012; Merloni et al. 2014), and the host galaxy star formation rate (SFR) does not distinguish X-ray-selected AGNs with different obscuring column densities (e.g., Rosario et al. 2012; Rovilos et al. 2012; Merloni et al. 2014).

Nonetheless, the measurements of SF properties for quasar host galaxies still suffer from selection biases that are often different among various quasar populations. In particular, optical and X-ray-selected quasar samples might have different completeness in obscured and unobscured sources due to the attenuation of optical and X-ray radiation by dust and gas. In fact, some studies have suggested that optical surveys might miss  $\sim 50\%$  of the AGN population due to both the obscuration and host galaxy contamination in low-luminosity AGNs (e.g., Goulding & Alexander 2009; Goulding et al. 2011a). While current X-ray observations probing photons with energy at  $\sim 10$  keV are believed to be less affected by moderate levels of obscuring materials ( $N_{\text{H}} < 10^{24} \text{ cm}^{-2}$ ), a significant fraction of X-ray AGNs ( $\sim 20 - 50\%$ , e.g., Donley et al. 2005; Guainazzi et al. 2005; Park et al. 2010; Alexander et al. 2011;

<sup>11</sup> In this work, we use AGNs as a general nomenclature for all energetically relevant SMBHs. For AGNs with bolometric luminosity larger than  $\sim 10^{45} \text{ erg s}^{-1}$ , we refer to them as quasars (QSOs).

Georgantopoulos et al. 2013; Wilkes et al. 2013) might still be missed due to obscuration that is Compton-thick ( $N_{\text{H}} \sim 10^{24} \text{ cm}^{-2}$ ). Although very hard X-ray photons can penetrate Compton-thick obscuration, the previous high-energy X-ray surveys are limited to local sources due to the shallow flux limits (e.g., *Swift*/BAT, Burlon et al. 2011 and *INTEGRAL*, Sazonov et al. 2012). While the *NuSTAR* (Harrison et al. 2013) mission opened a new window of high-energy X-ray up to 80 keV, the recent studies that used *NuSTAR* to observe heavily obscured AGNs have found that obscuration is still a nonnegligible effect, even for X-ray photons at such high energy (Lansbury et al. 2014; Stern et al. 2014).

In contrast, mid-IR observations of the reprocessed emission from the obscuring dust can detect heavily obscured AGNs. A number of studies have shown that large populations of AGNs can be selected using the power-law spectral energy distribution (SED) shape of AGNs at mid-IR wavelengths (e.g., Lacy et al. 2004; Stern et al. 2005; Hickox et al. 2007; Assef et al. 2010b; Donley et al. 2012). Although these mid-IR color selection criteria cannot avoid some star-forming galaxy interlopers and might miss AGNs accreting at lower accretion rates (e.g., Hickox et al. 2009; Donley et al. 2012; Mateos et al. 2013; Chung et al. 2014; Hainline et al. 2014) or AGNs with complicated silicate features in their mid-IR SED (Kirkpatrick et al. 2013), they are effective in selecting both obscured and unobscured AGNs with similar completeness in mid-IR wavelengths. Recent studies have shown that mid-IR-selected AGNs can also be separated into obscured and unobscured populations using a simple optical to mid-IR color selection criterion (e.g., Hickox et al. 2007; DiPompeo et al. 2014; Donoso et al. 2014), which can easily be explained by the different level of extinction in the optical emission from the nucleus (e.g., Hickox et al. 2007, H07 hereafter). Therefore, a direct comparison of the host galaxy SF properties of obscured and unobscured sources in a mid-IR-selected quasar sample can provide insights to the origin of obscurations in rapidly accreting SMBHs.

In this work, we adopt the mid-IR-selected quasar sample from Hickox et al. (2011, H11 hereafter), which is comprised of unobscured and obscured quasars with similar distributions in quasar properties (e.g., redshift and quasar luminosity), thus making it an excellent sample to study the connection between host galaxy properties and quasar obscuration. The quasar sample studied in this work consists of 546 unobscured quasars (QSO1s) and 345 obscured quasars (QSO2s) selected using *Spitzer* mid-IR observations in the Boötes survey region. We utilize the optical spectroscopy from the AGN and Galaxy Evolution Survey (AGES, Kochanek et al. 2012) and the XBoötes *Chandra* X-ray observations (Murray et al. 2005), along with the 250  $\mu\text{m}$  data from the Spectral and Photometric Imaging Receiver (SPIRE, Griffin et al. 2010) on board the *Herschel Space Observatory*. With the inclusion of the far-IR photometry in which AGN contributions have been shown to be much smaller than that of the host galaxy (e.g., Netzer et al. 2007; Lacy et al. 2007a; Kirkpatrick et al. 2012; Mullaney et al. 2012; Chen et al. 2013; Del Moro et al. 2013; Drouart et al. 2014), we can use the wealth of multiwavelength observations in the Boötes field to obtain robust measurements of SFR for luminous quasars and test if they are associated with obscuration.

We also take advantage of this sample to study the correlation between star formation and AGN accretion for the

mid-IR QSOs. In galaxy evolution models, which suggest that the concurrent growth of AGN and host galaxy occurs during the dust-enshrouded galaxy merger phase, different types of quasars represent different stages of galaxy evolution. To date, observational studies on the connection between SFR and AGN accretion rate have not yet shown definitive conclusions. Positive, strong correlations have been found in studies of optically selected type I quasars (e.g., Serjeant & Hatziminaoglou 2009) and type II quasars (e.g., Netzer 2009), while different conclusions have been found in X-ray-selected quasars at higher redshift (e.g., Silverman et al. 2009; Mullaney et al. 2012; Rosario et al. 2012). The difference between observed correlations could be driven by various limitations and observational constraints such as sample size (Harrison et al. 2012; Page et al. 2012) or AGN intrinsic variability (e.g., Chen et al. 2013; Hickox et al. 2014). In addition, it is also important to note that AGNs selected with different criteria are hosted by very different host galaxy populations (e.g., Hickox et al. 2009; Griffith & Stern 2010; Goulding et al. 2014) in which the galaxy and SMBH might follow different evolutionary paths. The sample in this work consists of a large number of luminous QSOs, including both the unobscured and heavily obscured populations; thus biases due to small-number statistics and the exclusion of dust-enshrouded AGNs are small. The bias in the observed SFR–AGN accretion rate relation in AGN host galaxies due to short-term AGN accretion rate stochasticity may also be less significant in luminous quasars (Hickox et al. 2014). Therefore, the SFR–AGN accretion rate correlation for the mid-IR-selected quasar populations may shed light on the origin of the concurrent growth of SMBH and galaxy.

This paper is organized as follows: in Section 2 we describe the multiwavelength data and the properties of the quasar sample. In Section 4, we discuss the SED-fitting procedures that we used to disentangle the AGN and the host galaxy contributions. In Section 3, we explore details of the observed far-IR properties of QSO1s and QSO2s. A comparison of the SF luminosity between QSO1s and QSO2s is laid out at Section 5. The X-ray properties for the QSO2s are discussed in Section 6, and the AGN obscured fraction as a function of SF luminosity is discussed in Section 7. A discussion and a summary are given in Section 8. Throughout the paper, we use the Vega magnitude system and assume a  $\Lambda$ CDM cosmology with  $\Omega_m = 0.3$ ,  $\Omega_\Lambda = 0.7$  and  $H_0 = 70 \text{ km s}^{-1}$ .

## 2. QUASAR SAMPLE

In this section, we discuss the data from the Boötes survey region as well as the quasar selection and classification criteria we adopted.

### 2.1. Data

The sample studied in this work comes from the 9 deg<sup>2</sup> Boötes survey region covered by the NOAO Deep Wide-Field Survey (NDWFS, Jannuzi & Dey 1999). Boötes is unique among extragalactic surveys because of its large area and the excellent multiwavelength coverage from space- and ground-based telescopes, which make possible statistical study of the rare luminous AGNs.

In this work, we use the multiwavelength photometry catalog from Brown et al. (private communication), which is the same as the one used in Chung et al. (2014). This catalog covers the optical to mid-IR bands, including the NDWFS optical

observations in the  $B_w$ ,  $R$ , and  $I$  bands, near-IR photometry from the NOAO NEWFIRM survey ( $J$ ,  $H$ , and  $K_s$ , Gonzalez et al. 2010), and the *Spitzer* Deep Wide Field Survey (SDWFS, Ashby et al. 2009) of the four bands of mid-IR observations from the *Spitzer* Infrared Array Camera (*IRAC*) at 3.6, 4.5, 5.8, and 8  $\mu\text{m}$ . In addition, the mid-IR photometry from the *Spitzer* Multi-band Imaging Photometer (*MIPS*) at 24  $\mu\text{m}$  is also included (IRS GTO team, J. Houck (PI), and M. Rieke). In this catalog, the optical to near-IR photometry was extracted from a matched aperture for each band. For the  $B_w$ ,  $R$ ,  $I$ ,  $H$ , and  $K_s$  bands, the photometry was measured from images smoothed to a common point-spread function (PSF) with a  $1''.35$  FWHM; while for the  $J$  band, the photometry was measured from images smoothed to a common PSF with a  $1''.60$  FWHM. To ensure consistency in the photometry, we use  $6''$  aperture photometry from optical bands through the *IRAC* bands in the mid-IR to account for the large *IRAC* beam size. For the *MIPS* data, we use PSF photometry instead of aperture photometry due to the still larger beam size of *MIPS*. The  $5\sigma$  flux limits of the optical to near-IR broadband photometry are 25.2, 23.9, 22.9, 21.1, 20.1, and 18.9 (Vega magnitudes) for the  $B_w$ ,  $R$ ,  $I$ ,  $J$ ,  $H$ , and  $K_s$  bands, respectively. For the mid-IR wavelengths, the  $5\sigma$  flux limits are 6.4, 8.8, 51, 50, and 170  $\mu\text{Jy}$  for the 3.6, 4.5, 5.8, 8.0, and 24  $\mu\text{m}$  bands, respectively. An extensive description of the multiband photometry extraction can be found in Brown et al. (2007).

We also make use of the far-IR observations from the publicly available *Herschel* Multi-tiered Extragalactic Survey (HerMES, Oliver et al. 2012). We rereduced and mosaiced the Boötes SPIRE observations (Alberts et al. 2013), which include a deep  $\sim 2$  deg<sup>2</sup> inner region near the center of the field and a shallower  $\sim 8.5$  deg<sup>2</sup> outer region. We specifically focused on removing striping, astrometry offsets, and glitches missed by the standard pipeline reduction. We also convolved the raw maps with a matched filter (see Chapin et al. 2011), which aided in source extraction by lowering the overall noise and deblending sources. From this we generated a matched filter catalog with a  $5\sigma$  detection threshold. In this catalog, we consider SPIRE sources with fluxes larger than 20 mJy as unambiguously detected. Completeness simulations show that these catalogs are 95% complete in the inner region and 69% complete in the outer regions above a flux of 20 mJy. We also find minimal flux boosting for low-SNR sources above this flux cutoff (see Section 2.2 in Alberts et al. 2013 for the details of the completeness simulation). We match the positions of the SPIRE catalog to the  $I$ -band positions with a matching radius of  $5''$ . We tested the rate of spurious matches by offsetting the SPIRE source positions by  $1'$  in a random direction and matching the randomly shifted catalog to the Boötes catalog. We found that with a radius of  $5''$ , our matching between the SPIRE and Boötes catalog only yielded  $<2\%$  spurious matches.

In addition, we also match the positions of the Brown et al. (2007) catalog to the publicly available *Wide-field Infrared Survey Explorer* (*WISE*) All-sky catalog (Wright et al. 2010) and obtain the profile-fit photometry magnitudes in the  $W1$ ,  $W2$ ,  $W3$ , and  $W4$  bands (3.4, 4.6, 12, and 22  $\mu\text{m}$ ).

As a complementary measurement of the AGN accretion rate and absorption by gas, we utilize X-ray data from the XBoötes survey, which is a mosaic of 126 short (5 ks) *Chandra* ACIS-I images (Kenter et al. 2005; Murray et al. 2005) covering the entire NDWFS. XBoötes contains 3,293 X-ray point sources

with at least four counts in the AGES survey region. The conversion factors from count rates (in counts  $\text{s}^{-1}$ ) to flux (in erg  $\text{s}^{-1}$ ) for the XBoötes are  $6.0 \times 10^{-12}$  erg  $\text{s}^{-1}$  count<sup>-1</sup> in the 0.5–2 keV band and  $1.9 \times 10^{-11}$  erg  $\text{s}^{-1}$  count<sup>-1</sup> in the 2–7 keV band, which are derived for a 5 ks on-axis observation and assuming a canonical unabsorbed AGN X-ray spectrum (see Section 3.3 of Kenter et al. 2005).

For this study, we use spectroscopic redshifts (*spec-zs*) from AGES when possible. For the sources without a *spec-z*, we adopt the photometric redshifts (*photo-zs*) calculated using techniques combining artificial neural network and template-fitting algorithms (Brodwin et al. 2006). The uncertainty of this set of *photo-zs* is  $\sigma = 0.06(1+z)$  for galaxies and  $\sigma = 0.12(1+z)$  for AGNs. We note that the uncertainties for AGNs are dominated by the difference between *photo-zs* and *spec-zs* for the type I AGNs. The uncertainties in the *photo-zs* for QSO2s are difficult to estimate accurately, as only 9% of the QSO2s have *spec-z* measurements. For these 32 QSO2s, the uncertainty of the *photo-zs* is  $\sigma = 0.06(1+z)$ , which is consistent with the uncertainty for the galaxy population. Recently, spectroscopic follow-up of 35 *WISE*-selected, optically obscured quasars by Hainline et al. (2014) also found a *photo-z* derived from a template-based algorithm (Assef et al. 2010a) with a similar accuracy. This is not surprising, since the optical SED for the heavily obscured AGNs is dominated by the host galaxy, which has more spectral features and should allow for a more accurate *photo-z* measurement.

An upper limit for the QSO2 *photo-z* uncertainties can be estimated based on different approaches. H07 obtained an uncertainty of  $\sigma_z = 0.25(1+z)$  by comparing the Brodwin et al. 2006 *photo-zs* to the *photo-zs* estimated by fitting three different galaxy templates to the  $B_w$ ,  $R$ ,  $I$  photometry. Since the accuracy of the *photo-zs* based on fitting three galaxy templates to three optical photometric observations is limited, the  $\sigma_z = 0.25(1+z)$  uncertainty is a very conservative upper limit. For this study, we adopt the *photo-z* uncertainty upper limit of  $\sigma_z = 0.25(1+z)$  from H07. However, this is a very conservative estimate, since the *photo-z* uncertainties for the QSO2s with host-galaxy-dominated optical SEDs are likely to be much smaller. A full discussion of the *photo-z* uncertainties is given in Section 8.

## 2.2. AGN Identification and Classification

The AGNs in this work are drawn from the quasar sample of H11, which is a subset of quasars from the H07 mid-IR AGN sample. The H07 AGNs were identified based on the *IRAC* color-color selection criterion of Stern et al. (2005). For the redshift range of the H07 sample ( $0.7 < z \lesssim 3.0$ ), the *IRAC* filters probe wavelengths at which the characteristic power-law continuum from the reprocessed AGN radiation starts to dominate. At these wavelengths, the light from old stellar populations is characterized by a Rayleigh–Jeans tail of a blackbody radiation with temperature higher than 2,500 K, which peaks at wavelengths different from both the AGN accretion disk and the reprocessed AGN emission. In addition, dust emission at near-sublimation temperature heated by the AGN is significantly stronger than that heated by massive stars; thus AGNs can be easily identified by their mid-IR color (e.g., Lacy et al. 2004; Stern et al. 2005; Donley et al. 2012). These reprocessed photons at mid-IR wavelengths are less affected by obscuration than the optical and the X-ray photons due to their

much smaller absorption cross section. Therefore, even heavily obscured AGNs can be identified using mid-IR selection criteria.

An important feature of the H07 catalog is that the AGNs were selected from the IRAC Shallow Survey (ISS, Eisenhardt et al. 2004), which has shallower flux limits than the later SDWFS survey. While the Stern et al. (2005) AGN selection can be contaminated by SF galaxies in deep mid-IR surveys (e.g., Donley et al. 2012), the contamination is negligible at the shallow flux limits of ISS (see Hickox et al. 2007; Assef et al. 2010a; Assef et al. 2011).

H07 also showed that the distribution of the optical ( $R$ ) band to mid-IR ( $4.5 \mu\text{m}$ ) colors is bimodal for the luminous mid-IR quasars. This bimodality can be easily explained by the difference between the SEDs of unobscured and obscured quasars. For mid-IR-selected quasars, the AGN dominates the mid-IR wavelengths, while for obscured quasars, the nuclear emission at optical wavelengths is heavily absorbed. Thus the SED in the  $R$  band for obscured quasars is similar to those of normal galaxies (e.g., Polletta et al. 2006; Hickox et al. 2007, and R. Hickox et al. 2015 in preparation). H07 has shown that the mid-IR-selected quasars can be separated into two distinct populations of quasars with an empirical color cut at  $R - [4.5] = 6.1$ . Most ( $\sim 80\%$ ) of the quasars in H07 with  $R - [4.5] < 6.1$  are spectroscopically confirmed as type 1 quasars; therefore in this work we refer to these unobscured quasars with  $R - [4.5] < 6.1$  as QSO1s. As for quasars with  $R - [4.5] > 6.1$ , due to the limited depth of AGES, only  $\sim 5\%$  have spectroscopic measurements and can be classified as type 2 quasars spectroscopically. However, H07 have extensively studied the quasars with  $R - [4.5] > 6.1$  and have shown that these quasars are consistent with bright, obscured X-ray AGNs with  $N_{\text{H}} > 10^{22} \text{ cm}^{-2}$  and with AGN bolometric luminosities  $L_{\text{AGN}} > 10^{45} \text{ erg s}^{-1}$ . Therefore, we refer to the obscured quasars with  $R - [4.5] > 6.1$  as QSO2s.

This empirical classification based on the quasar mid-IR to optical color has been shown to be broadly consistent with both the spectroscopically classified sources (Donoso et al. 2014) and the X-ray hardness ratio (defined as  $\text{HR} = (H - S)/(H + S)$ , where  $H$  and  $S$  are the photon counts in the 2–7 keV band and 0.5–2 keV band, respectively) classification criteria (Hickox et al. 2007; Usman et al. 2014). Since we lack spectroscopic confirmation for the majority of the QSO2s, it is possible that the QSO2s are different from the optical type 2 quasars. Recently, Lacy et al. (2013) have also studied the optical and near-IR spectroscopy of mid-IR AGNs selected using the Donley et al. (2012) IRAC color criteria and found that a significant fraction ( $\sim 33\%$ ) of the AGNs with evident mid-IR power-law continuum have no significant emission lines consistent with the optical emission line diagnostics (e.g., Baldwin et al. 1981), suggesting that these mid-IR obscured AGNs are more deeply obscured than the optically selected type 2 AGNs. This has also been suggested by the recent study of Hainline et al. (2014).

### 2.3. Final Sample

To minimize the uncertainty in the measurements of quasar and host galaxy properties due to the scattering in the *photo-zs*, we focus on the H11 quasar sample, which is a subsample from H07. The H11 quasar sample focuses on the redshift range  $0.7 < z < 1.8$  and limits the QSO1s to those with broad optical emission lines and robust *spec-z* measurements from AGES. For the QSOs in this redshift range, all of the sources have  $I < 18$ , and the spectroscopic QSO1 sample is highly complete.

For the QSO2s in this redshift range, only 32 ( $\sim 9\%$ ) of the QSO2s have *spec-z* measurements. For the rest of the QSO2s, we adopt the *photo-zs* from Brodwin et al. (2006). This subset of QSOs have been used in the study of clustering properties of QSO1s and QSO2s in H11, which showed that in the redshift range  $0.7 < z < 1.8$ , the sample is highly complete at the shallow flux limits of ISS. The mid-IR selection of this particular sample is shown to suffer less than  $< 20\%$  contamination from star-forming galaxies (Hickox et al. 2011). Since the purpose of this work is to compare the star formation properties of QSO1s and QSO2s, it is important to make sure that any difference in SF properties is not driven by the presence of starburst galaxy interlopers. Additionally, even for bright mid-IR quasars the starburst contribution in the MIR may be nonnegligible. Therefore, we rely on SED decompositions to disentangle the AGN and starburst components. The details of the SED decomposition are laid out in Section 3. Our SED-fitting results show that all of the H11 QSOs have a nonnegligible ( $> 20\%$ ) AGN component. Based on the SED-fitting results,  $\sim 3\%$  of the H11 QSOs would have  $L_{\text{AGN}}$  less than the QSO criterion ( $L_{\text{AGN}} > 10^{45} \text{ erg s}^{-1}$ ). We therefore limit our focus to the sample of 546 QSO1s and 345 QSO2s that satisfies the QSO luminosity criterion and comprises  $\sim 97\%$  of the H11 sample.

As a demonstration of the sample used in this work, we show the distribution of the IRAC  $[3.6] - [4.5]$  to  $[5.8] - [8.0]$  colors and the  $R - [4.5]$  to  $L_{\text{AGN}}$  distributions of the quasar sample in Figure 1. We note that in Figure 1(a), a small number of the H07 sources have  $[3.6] - [4.5]$  and  $[5.8] - [8.0]$  colors that lie outside the Stern et al. (2005) AGN selection wedge. The Stern et al. (2005) AGN selection wedge and the H07 sample were defined using the original ISS catalog in which the mid-IR photometry was derived using the standard aperture correction, which is different from the PSF profile-fitting corrections for individual sources in the Brown et al. (2007) catalog. Moreover, the updated IRAC photometry comes from SDWFS, which is two times deeper than the ISS. Thus, it is not surprising that a small fraction ( $\sim 4\%$ ) of the original H07 sample does not meet the original Stern et al. (2005) criterion. However, the QSO sample in Figure 1(a) shows a tight  $[5.8] - [8.0]$  to  $[3.6] - [4.5]$  distribution, which is not seen in the similar Figure 1(a) of H11, which uses the original ISS photometry. This suggests that the majority of our sample does have power-law-like mid-IR SED with the high-precision photometry of SDWFS (e.g., see Figure 22 in H07). For the purpose of completeness we do not exclude the sources outside of the updated AGN selection wedge, since these sources might still have a nonnegligible AGN component that can be identified by the SED fits. However, we note the exclusion of this small fraction of sources has little effect on the average properties of the QSOs. We also show the redshift and flux distributions of the sample in Figure 2, which shows that the redshift distributions of the QSO1s and QSO2s are similar.

### 3. SED DECOMPOSITION

Although it is now well-established that far-IR fluxes at wavelengths longer than  $60 \mu\text{m}$  in AGN host galaxies are mostly dominated by the emission related to SF (e.g., Netzer et al. 2007; Mullaney et al. 2011; Rosario et al. 2012), caution is still required when estimating the SF properties of powerful quasars. Here we use SED decompositions to ensure that we

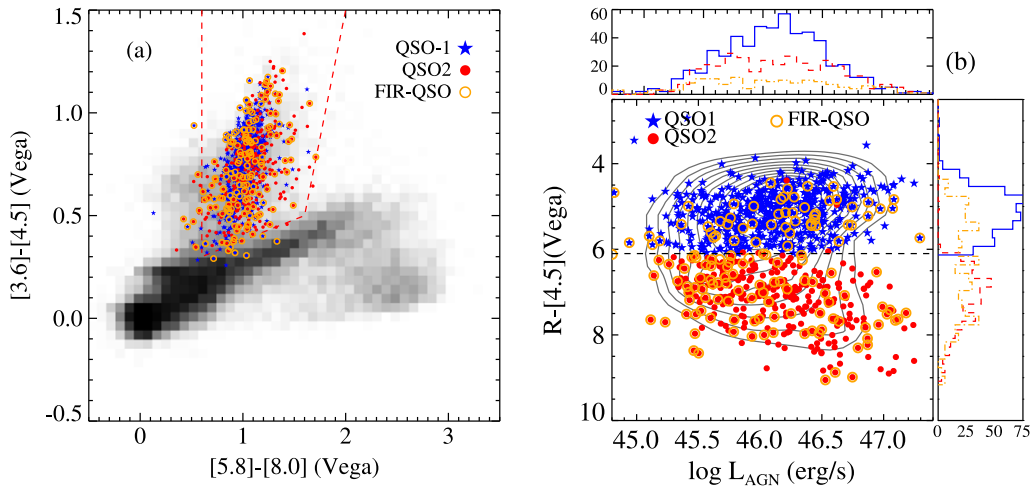


**Figure 1.** (a) *IRAC* color-color diagram showing the selection of the quasar samples using the criteria of Stern et al. (2005). The gray-scale shows the density of sources detected at  $>5\sigma$  significance in all four bands in the SDWFS data. Blue stars and red circles show the QSO1 and QSO2 samples, respectively. The Stern et al. (2005) color-color selection region is shown by the dashed line. In addition, the QSOs with far-IR detections (FIR-QSO) are enclosed with orange circles. Some of the mid-IR QSOs fall out of the selection wedge due to the updated *IRAC* photometry and aperture corrections (see Section 2.3). (b) Illustration of the optical-IR color-selection criteria for dividing the IR-selected QSO sample into unobscured (QSO1) and obscured (QSO2) subsamples. Shown is the observed  $R - [4.5]$  color versus bolometric luminosity, calculated as described in Section 4. Contours show the distribution for all the Hickox et al. (2007) IR-selected quasars, while blue stars and red circles show the QSO1 and QSO2 subsamples at  $0.7 < z < 1.8$  used in H11 and this analysis, as described in Section 2. The distribution in the  $R - [4.5]$  color and  $L_{\text{AGN}}$  are also shown as histograms in the side panels. QSO1s are shown as the blue solid lines, QSO2s are shown as the red dashed lines, and the FIR-QSOs are shown as the orange dash-dotted lines. The contours and color histograms show that a simple cut in optical-IR color clearly separates the QSO samples into two populations.

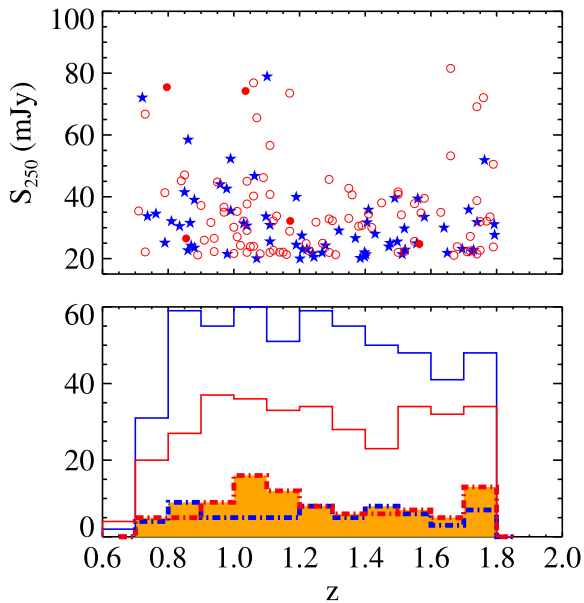


**Figure 2.** Top: the  $250\ \mu\text{m}$  distributions for QSO1s and QSO2s with direct SPIRE detections. QSO1s are shown as the blue stars. The five far-IR-detected QSO2s with *spec-z* measurements are shown as the filled circles. The rest of the far-IR-detected QSO2s with *photo-z*s are shown as open circles. Bottom: the redshift distributions of QSO1s and QSO2s are shown in blue and red solid lines. Also shown are the redshift distributions of the QSO1s and QSO2s detected at  $250\ \mu\text{m}$ . The histograms for far-IR-detected QSO1s and QSO2s are shown as the blue and red dash-dotted lines and filled in orange. This plot shows that the redshift distributions of QSO1s and QSO2s are similar, and QSO2s have more  $250\ \mu\text{m}$  detections than QSO1s.

have reliable estimates of the intrinsic AGN luminosity ( $L_{\text{AGN}}$ ) and star formation luminosity ( $L_{\text{SF}}^{\text{IR}}$ ).<sup>12</sup>

<sup>12</sup> Defined as the integrated  $8-1000\ \mu\text{m}$  luminosity of the host galaxy component only.

To properly disentangle the emission from stars and AGN accretion, we fit all of the available broadband photometry in our data sets with SED templates. We combine several empirically derived templates to create AGN and host galaxy templates covering the wavelength range from optical to far-IR in our data (see Section 3.1).

### 3.1. SED Templates

Our SED-fitting procedures utilize the four empirical SED templates spanning  $0.03-30\ \mu\text{m}$  described in Assef et al. (2010a, A10 hereafter). A10 have shown that the nonnegative combinations of three different galaxy templates and a single AGN template, with the addition of extinction to the AGN component only, can robustly describe the optical to mid-IR SEDs of a wide variety of AGNs selected using *Spitzer IRAC* color (Assef et al. 2010a) or *WISE* color (Assef et al. 2010b; Chung et al. 2014). However, these templates do not include the far-IR wavelengths that are crucial for this work.

To extend the A10 AGN template to the far-IR, we create ad hoc AGN templates by replacing the hot-dust component of the A10 AGN template with the average infrared quasar template from Netzer et al. (2007) and the three infrared AGN templates (for low-, mean-, and high-luminosity AGNs) from Mullaney et al. (2011), which cover a wide range of AGNs with different mid-IR to far-IR properties. This is based on the assumption that the SED of the hot accretion disk around the SMBH is the same for all the radiatively efficient AGNs and that the differences are due to variable extinction and different spectral shapes in the mid- and far-IR wavelengths due to different distributions of dust. To account for the extinction at the AGN templates, we use the Draine (2003) extinction law with  $R_V = 3.1$ , which mainly attenuates the SED at  $\lambda \leq 30\ \mu\text{m}$  and also produces the silicate absorption features at mid-IR wavelengths that are common among AGN. The extinction strength is treated as a free parameter with a range of  $0 < A_V < 48$ .

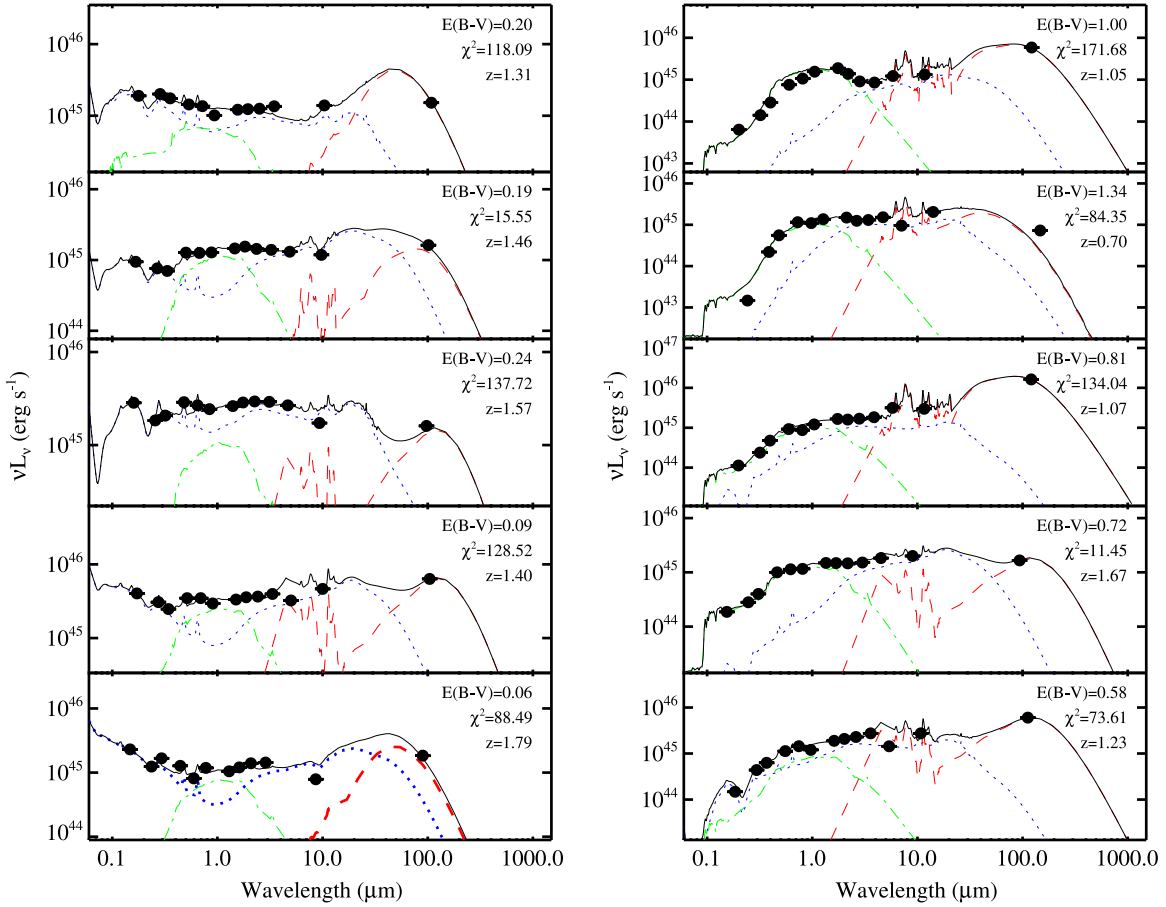


**Figure 3.** Examples of the best-fit SEDs (solid line) in the rest-frame of each source. These sources are fitted using an AGN component with a Draine (2003) extinction law (dotted curve), an empirical stellar component (dash-dotted), and empirical starburst templates (dashed). We find that almost all sources have an SED dominated by the starburst component in the far-IR; see Section 3 for details.

For the host galaxy templates, we consider two different components: the contribution from the stellar population of the galaxy, which accounts for the optical to near-IR emission, and a starburst component, which represents the mid- to far-IR dust emission from reprocessed stellar light. For the stellar population component, we follow the approach described in A10 by assuming that the stellar population in any galaxy is comprised of the nonnegative combination of the three empirical galaxy templates with populations of starburst (Im), continuous star-forming (Sbc), and old stars (elliptical), respectively (Assef et al. 2008; 2010a). Unlike the elliptical template, the Sbc and Im templates both contain hot-dust components in addition to the stellar population SEDs. Since the dust component does not extend to the far-IR wavelengths that we require and will be taken into account in the starburst templates, which we will choose later on, we replace the dust emission ( $\lambda > 4.9 \mu\text{m}$ ) in the Sbc and Im templates with the SED identical to the elliptical galaxy to create empirical stellar population templates with no dust emission. At these wavelengths the stellar SEDs are dominated by low-mass stars similar to the elliptical template. For our mid-IR-selected quasar sample, the starlight contribution is negligible at the wavelengths where hot-dust emission dominates.

For the starburst component, we use the 105 starburst templates from Chary & Elbaz (2001) and the 64 starburst templates from Dale & Helou (2002). The Chary & Elbaz (2001) and Dale & Helou (2002) starburst templates cover a

wide range of SEDs for various prototypical local star-forming galaxies, with  $L_{\text{IR}}$  in the range between  $10^8 - 10^{13.5} L_{\odot}$ . For SF galaxies at  $z > 1$ , these templates have been shown to be reliable when used to estimate SF-related  $L_{\text{IR}}$  with monochromatic SPIRE observations (e.g., Elbaz et al. 2011). However, as pointed out by Kirkpatrick et al. (2012), the starburst galaxies at higher redshift have different dust temperatures and SED shapes. Although the effect of the different dust temperature on the estimation of  $L_{\text{IR}}^{\text{SF}}$  is small when the wavelengths of the SPIRE bands probe the peak of the cold-dust emission, it is still important to include high-redshift starburst templates to accommodate the possibly different SED shapes of high-redshift starbursts. Therefore, we also include the  $z \sim 1$  and  $z \sim 2$  average starburst SED templates from Kirkpatrick et al. (2012) in our SED-fitting analysis. We thus adopt a total of 171 starburst templates in our SED-fitting analysis.

Given these SED templates described above, we fit the observed photometry with an iterative  $\chi^2$  minimization algorithm (Levenberg–Marquardt) to minimize the function.

$$\chi^2 = \sum_{i=0}^{n_{\text{filters}}} \frac{F_{\text{obs},i} - aF_{\text{star},i} - b \text{ext}(E(B-V))F_{\text{AGN},i} - cF_{\text{starburst},i}}{\sigma_i^2} \quad (1)$$

Here  $F_{\text{obs},i}$  is the observed flux in the  $i$ th band and  $\sigma_i$  is its

**Table 1**  
Results of Far-IR Stacking Analysis

Average $f_{250}$ in Bins of $R-4.5$				
$R - [4.5]$ (Vega)	4.7	5.4	6.6	7.5
$S_{250}$ (mJy) (ND)	$6.5 \pm 0.73$	$7.9 \pm 0.59$	$7.3 \pm 0.75$	$8.5 \pm 1.00$
$S_{250}$ (mJy) (All)	$8.0 \pm 0.84$	$11. \pm 0.77$	$16. \pm 1.50$	$18. \pm 0.21$
$z$ (All)	1.31	1.20	1.19	1.31
Average $f_{250}$ in Bins of $L_{\text{AGN}}$				
$\log \langle L_{\text{AGN}} \rangle [\text{erg } s^{-1}]$	45.2	45.6	46.1	46.5
$S_{250}$ (QSO1)(mJy)	$3.7 \pm 0.82$	$5.4 \pm 0.70$	$5.2 \pm 0.75$	$7.7 \pm 0.95$
$S_{250}$ (QSO2)(mJy)	$3.5 \pm 0.94$	$8.8 \pm 1.40$	$5.1 \pm 0.66$	$8.4 \pm 2.70$
$z$ (Average)	0.98	1.17	1.36	1.49

**Notes.** Results from the far-IR stacking analysis described in Section 4.2. The top half of the table shows the results for sources binned in  $R - [4.5]$ . The first row shows the results for the far-IR nondetected (ND) sources only, and the second row shows the result for the entire QSO sample. The average redshift for all QSOs in each bin is also given. The bottom half of the table shows the results for the entire QSO1 and QSO2 samples binned in their AGN bolometric luminosity. The average redshift for each  $R - [4.5]$  and  $L_{\text{AGN}}$  bin is also listed; we note that there is only a  $<0.02$  average redshift difference between the QSO1s and QSO2s.

uncertainty.  $F_{\text{galaxy},i}$ ,  $F_{\text{AGN},i}$ , and  $F_{\text{starburst},i}$  are the fluxes of the stellar (optical), AGN (optical to far-IR), and starburst (far-IR) templates for filter  $i$ . The function  $\text{ext}$  gives the extinction of the AGN flux in band  $i$ , given the color excess  $E(B - V)$ . We optimize  $a$ ,  $b$ ,  $c$ , and  $E(B - V)$  to minimize the  $\chi^2$ .

### 3.2. Results

While uniform NUV to mid-IR photometric coverage is available for all of the sources in our sample, only  $\sim 18\%$  of them have a SPIRE 250  $\mu\text{m}$  detection with a flux larger than the 20 mJy. Since our sample is selected to have AGN-dominated mid-IR SED, the far-IR photometry is essential to constrain the average SF properties. For the sources with direct far-IR detections, we fit their multiwavelength photometry with the SED templates described in the previous section. For the 731 sources without direct far-IR detections, we use a stacking analysis to constrain their average far-IR flux.

We stack the QSOs without direct far-IR detections in bins of  $R - [4.5]$  (see Section 4.2) and bins of  $L_{\text{AGN}}$  (derived in H11 from interpolations between the *IRAC* photometry and the *MIPS* 24  $\mu\text{m}$  photometry). The uncertainty of the stacked flux is determined by bootstrap resampling. We created 10,000 random samples by drawing objects from the original samples with replacement until the number of objects in each random sample is the same as the number in the original sample. The uncertainty of the stacked flux is the variation in the stacked fluxes of the random samples. The details of the far-IR stacking analysis can be found in Section 3.1.1 of Alberts et al. (2013). The results of the stacking analysis are given in Table 1.

To estimate the average SF luminosity of the far-IR nondetected QSOs, we assume that their 250  $\mu\text{m}$  fluxes and 250  $\mu\text{m}$  flux uncertainties are equal to the averages found from the stacking analysis for the sources with similar values of both  $R - [4.5]$  and  $L_{\text{AGN}}$ . We find that for the majority of the SPIRE nondetected sample, the best-fit SED reproduces the observed average far-IR flux well.

From SED-fitting results with far-IR fluxes stacked in bins of  $R - [4.5]$  and  $L_{\text{AGN}}$ , we find that  $\sim 85\%$  of the quasars have a

prominent AGN hot-dust component (AGN component  $>50\%$ ) at mid-IR wavelengths covered by the *IRAC* bands. All of the quasars have a nonnegligible ( $>20\%$ ) AGN component, confirming that the H11 sample consists of powerful quasars. However, the AGN dominates the quasar SED even at 24  $\mu\text{m}$  for more than half of our sample. Therefore, the SF properties of these powerful quasars are primarily constrained by their far-IR photometry. For individual sources with only the stacked SPIRE flux to anchor the starburst component, this approach of using stacked far-IR flux can lead to inaccurate  $L_{\text{IR}}^{\text{SF}}$ . However, the main purpose of this work is not to determine the  $L_{\text{IR}}^{\text{SF}}$  for individual QSOs. Instead, we take this approach to constrain the AGN contamination in the average far-IR SF luminosity with the well-fitted mid-IR AGN SED, which can robustly determine the average  $L_{\text{IR}}^{\text{SF}}$  for different QSO populations. We note that when we compare the stacked fluxes from either the  $R - [4.5]$  bin or the  $L_{\text{AGN}}$  bin with the best-fit AGN component, we find that the average AGN contribution at 250  $\mu\text{m}$  is only 5%, and none of the QSOs in our sample have an AGN component that contributes more than 40% at 250  $\mu\text{m}$ . Since the average intrinsic SEDs for AGNs are expected to fall more rapidly in more luminous systems (Mullaney et al. 2011), a starburst component is essential to reproduce to average flux at 250  $\mu\text{m}$ . Examples of the best-fit SEDs are shown in Figure 3.

With the best-fit SEDs, we calculate the total infrared luminosity for each QSO ( $L_{\text{IR}}^{\text{tot}}$ ) by integrating the best-fit SEDs from 8 – 1000  $\mu\text{m}$ . For each source in our sample, we also calculate the  $L_{\text{IR}}$  of the starburst component by integrating the host galaxy component of the best-fit SED over the same wavelength range ( $L_{\text{IR}}^{\text{SF}}$  hereafter).<sup>13</sup> We find that for our sample, the average ratio between  $L_{\text{IR}}^{\text{SF}}$  and  $L_{\text{IR}}^{\text{tot}}$  is  $\sim 55\%$ , indicative of a nonnegligible AGN contribution to  $L_{\text{IR}}^{\text{tot}}$  in these mid-IR luminous quasars. This is also consistent with the Kirkpatrick et al. (2012) results of the study combining *Spitzer* IRS spectra and multiband *Herschel* photometry for  $z \sim 1$  and  $z \sim 2$  ULIRGs. However, the far-IR flux probed by the SPIRE 250  $\mu\text{m}$  band is dominated ( $>70\%$ ) by the starburst component for  $\sim 90\%$  of our sample. This result confirms that quasar SEDs are still dominated by a starburst component at rest-frame wavelengths longer than 100  $\mu\text{m}$  (e.g., Netzer et al. 2007; Mullaney et al. 2011; Rosario et al. 2012; Del Moro et al. 2013). Therefore, the average  $L_{\text{IR}}^{\text{SF}}$  of powerful mid-IR quasars can still be robustly measured with the inclusion of far-IR photometry.

We next derive the bolometric AGN luminosity ( $L_{\text{AGN}}$ ) by directly integrating the deabsorbed AGN component. We compare the  $L_{\text{AGN}}$  from our SED fitting with the  $L_{\text{AGN}}$  derived in H11 and find that our  $L_{\text{AGN}}$  is higher than the H11  $L_{\text{AGN}}$  by an average of  $\sim 0.1$  dex. Since the derivation of  $L_{\text{AGN}}$  in H11 did not correct for the weak but nonnegligible dust obscuration and SF galaxy contamination in the mid-IR, it is not surprising that our  $L_{\text{AGN}}$  is different. However, the difference is small due to the fact that most of the quasars in this sample are dominated by the AGN, and the dust obscuration only weakly attenuates the SED at mid-IR wavelengths. We show the redshift distributions of  $L_{\text{IR}}^{\text{tot}}$  and  $L_{\text{AGN}}$  in Figure 4.

<sup>13</sup> For clarification, we use  $L_{\text{IR}}$  as a general terminology for any integrated 8–1,000  $\mu\text{m}$  luminosity. Approximately 90% is the integrated  $L_{\text{IR}}$  of the best-fit SED, and  $L_{\text{IR}}^{\text{SF}}$  is the  $L_{\text{IR}}$  of the host galaxy component only.

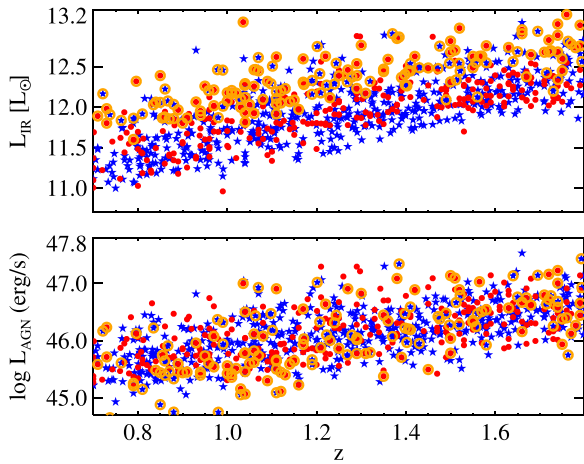


**Figure 4.** Redshift distributions of the (8–1,000  $\mu\text{m}$ )  $L_{\text{IR}}^{\text{total}}$  and the AGN bolometric luminosity derived from SED fitting and far-IR stacking for the nondetected sources described in Section 3.2. The symbols and lines represent the same subsets of objects shown in Figure 1, where blue stars and red circles are QSO1s and QSO2s, respectively. Individually, far-IR-detected sources (FIR–QSO) are enclosed with orange circles. In the top panel, the blue solid line, the red dashed line, and the orange dash-dotted line represent distributions of QSO1s, QSO2s, and FIR–QSOs, respectively.

#### 4. FAR-IR OBSERVATIONS AND QUASAR OBSCURATION

Several studies have pointed out that even for AGNs with quasar-like luminosities, their far-IR SEDs are often dominated by the cold-dust emission heated by young stars (e.g., Netzer et al. 2007; Lacy et al. 2007a; Kirkpatrick et al. 2012; Mullaney et al. 2012). Although alternative cases have been reported in some recent studies (e.g., Hiner et al. 2009; Dai et al. 2012), the cold temperature of the far-IR emission still requires the AGN-heated dust to reside at a large distance from the central SMBH (Sanders et al. 1988). In addition, powerful molecular outflows might also produce strong far-IR emission (e.g., Sun et al. 2014). However, the number of AGNs and starburst galaxies with confirmed warm molecular outflows from high-resolution far-IR or submillimeter observations is limited. Nonetheless, strong far-IR emission for quasars implies the existence of dust extending to a large distance well beyond the putative obscuring torus, and a comparison of far-IR properties between QSO1s and QSO2s could determine whether the quasar obscuration is related to the large-scale dust.

##### 4.1. SPIRE Detection Fraction

We begin with a very simple test by measuring the far-IR detection fraction above a flux limit of 20 mJy in the *Herschel* SPIRE 250  $\mu\text{m}$  filter ( $f_{250}$  hereafter) for QSO1s and QSO2s separately. In our survey region, the shallowness of the SPIRE observation implies that any quasars in our sample with a far-IR detection are at least as bright as luminous infrared galaxies (LIRGs, which are defined as galaxies with  $L_{\text{IR}}(8 - 1000 \mu\text{m}) > 10^{11} L_{\odot}$ ) at the same redshifts. At first glance, we find that among the 546 QSO1s, only 68 (12%) of them are detected in the SPIRE 250  $\mu\text{m}$  filter, while 102 of the 345 (29%) QSO2s have far-IR detections.

We next use  $R - [4.5]$  as a rough proxy of the obscuration strength on the nuclear emission and study whether  $f_{250}$  is related to the extinction at the  $R$  band. The primary goal of this

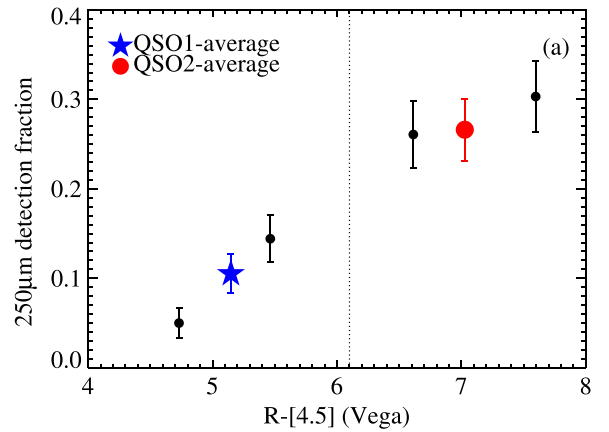


**Figure 5.** 250  $\mu\text{m}$  detection fraction ( $f_{250}$ ) as a function of the  $R - [4.5]$  color. The  $f_{250}$  for all QSO1s is shown as the blue star, and the  $f_{250}$  for all QSO2s (weighted to have a redshift and AGN bolometric luminosity distribution similar to that of QSO1s) is shown as the red circles. This figure shows that QSO2s are 2.4 times more likely to have a far-IR detection.

analysis is to study whether the star formation properties of the quasar-hosting galaxies are related to the observed obscuration. Therefore, it is important to make sure the QSO1s and QSO2s are matched in key properties, i.e., redshift and AGN bolometric luminosity ( $L_{\text{AGN}}$ , estimated from the SED-fitting analysis discussed in Section 3). We divide our sample into four bins of  $R - [4.5]$  and calculate  $f_{250}$  for each bin by applying statistical weights to each quasar so that the samples are matched in redshift and  $L_{\text{AGN}}$  in each bin. We find that the weighted  $f_{250}$  increases rapidly with  $R - [4.5]$  for QSO1s. For QSO2s,  $f_{250}$  is only weakly correlated with  $R - [4.5]$ , but the  $f_{250}$  of QSO2s is higher than that of QSO1s by a factor of  $2. \pm 0.2$ . We show the  $f_{250}$  to  $R - [4.5]$  relation in Figure 5.

##### 4.2. Average SPIRE 250 $\mu\text{m}$ Fluxes

Due to the flux limit of the SPIRE catalog,  $f_{250}$  only reflects the fraction of QSOs hosted by galaxies with very luminous far-IR emission. To extend this analysis, we estimate the average 250  $\mu\text{m}$  flux in bins of  $R - [4.5]$  to test if the far-IR flux of our quasar sample also evolves with  $R - [4.5]$ . To measure the average 250  $\mu\text{m}$  flux ( $S_{250}$ ) for all QSOs, we first estimate the average 250  $\mu\text{m}$  flux for the sources without direct SPIRE observations, using the stacking analysis discussed in Section 3.2. Next, the stacked fluxes are combined with the sources individually detected in the far-IR to calculate the average  $S_{250}$  for all QSOs. We show the average 250  $\mu\text{m}$  flux ( $S_{250}$ ) in the same  $R - [4.5]$  bins used for Figure 5, with results given in Table 1.

From the stacking analysis, we find that for QSOs without direct far-IR detections, there is no significant dependence of the average  $S_{250}$  on  $R - [4.5]$ . However, the mean  $S_{250}$  of the individually detected far-IR sources shows a  $R - [4.5]$  dependence similar to that of  $f_{250}$ . Therefore, driven by the increasing fraction of far-IR luminous sources, the average  $S_{250}$  of the entire QSO sample is correlated with  $R - [4.5]$ .

This result shows that for powerful mid-IR quasars with more dust attenuation at optical wavelengths, the average far-IR emission is stronger. This implies that at least part of the obscuration seen in the obscured QSOs might be due to the far-IR-emitting dust.

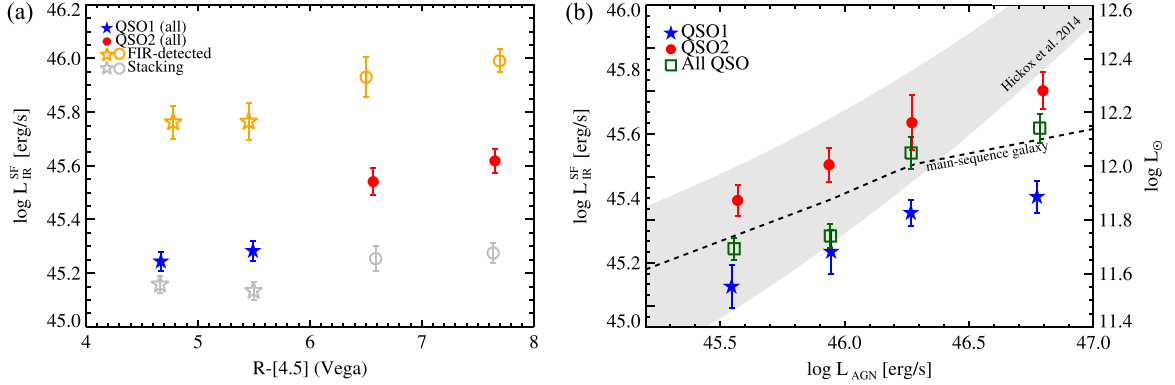


**Figure 6.** (a) Left: the relationship between  $L_{\text{IR}}^{\text{SF}}$  and  $R - [4.5]$  for the mid-IR-selected QSOs. Far-IR-detected QSOs are shown by the orange, open symbols, and the stacking results for the far-IR nondetected QSOs are shown by the gray, open symbols. In both cases, there is only a marginal increase in  $L_{\text{IR}}^{\text{SF}}$  with  $R - [4.5]$ . However, driven by the much higher far-IR detection fraction in QSO2s, the average  $L_{\text{IR}}^{\text{SF}}$  for QSO2s is higher than the average  $L_{\text{IR}}^{\text{SF}}$  for QSO1. (b) Right: the average  $L_{\text{IR}}^{\text{SF}}$  for QSOs in bins of  $L_{\text{AGN}}$ . The results for QSO1s are shown as the filled blue stars, while the results for QSO2s are shown as the filled red circles. For the entire QSO population, we also show their average  $L_{\text{IR}}^{\text{SF}}$  in four bins of  $L_{\text{AGN}}$  as the open green squares. For comparison, we show the Hickox et al. (2014) model evaluated at  $0.7 < z < 1.8$  as the shaded region. We note that the average redshift in each bin increases with  $L_{\text{AGN}}$ , and the relationship between  $\langle L_{\text{IR}}^{\text{SF}} \rangle$  and  $L_{\text{AGN}}$  is consistent with the redshift evolution for main-sequence SF galaxies with  $M_* = 10^{11} M_{\odot}$ . We show the redshift evolution of MS galaxies as the dashed line. The  $L_{\text{IR}}^{\text{SF}}$  for all QSOs coincides with the evolution of MS galaxies, suggesting a connection between QSO host galaxies and MS star-forming galaxies (see Section 5.2).

## 5. AVERAGE $L_{\text{IR}}^{\text{SF}}$ OF QSO1S AND QSO2S

In Section 3, we found that QSO2s have higher  $f_{250}$  and  $S_{250}$  than QSO1s. In this section, we examine whether the observed difference in the average far-IR fluxes of QSO1s and QSO2s can be associated with the difference in the star formation properties of their host galaxies, as predicted by the galaxy evolution models with a connection between quasar obscuration and star formation.

We first calculate the median star formation luminosity by averaging the  $L_{\text{IR}}^{\text{SF}}$  derived from SED fitting (Section 4). We find that for QSO1s, the mean  $L_{\text{IR}}^{\text{SF}}$  is  $10^{45.29 \pm 0.03} \text{ erg s}^{-1}$  ( $10^{11.71} L_{\odot}$ ), and for QSO2s, the mean  $L_{\text{IR}}^{\text{SF}}$  is  $10^{45.59 \pm 0.04} \text{ erg s}^{-1}$  ( $10^{12.01} L_{\odot}$ ). We find that similar to  $f_{250}$  and the average  $S_{250}$ , the median  $L_{\text{IR}}^{\text{SF}}$  for QSO2s is significantly higher than that of QSO1s by 0.30 dex. The higher  $L_{\text{IR}}^{\text{SF}}$  in QSO2s confirms the results from Section 3 that QSO2s are associated with host galaxies with more star-forming cold dust, which might be obscuring the nuclear emission.

### 5.1. $L_{\text{IR}}^{\text{SF}}$ versus $R - [4.5]$

To further study the relation between AGN obscuration and  $L_{\text{IR}}^{\text{SF}}$ , we divide our QSO sample into bins of  $R - [4.5]$  as a proxy for AGN obscuration. To be consistent with Section 3.1 and avoid the uncertainties by the lack of *spec-zs* of QSO2s, we opt to use  $R - [4.5]$  instead of the  $E(B - V)$  derived from SED fitting as the proxy for nuclear obscuration, since the uncertainties of the *photo-z* limit the accuracy of our ability to measure  $E(B - V)$ . We calculate the median AGN contribution at observed-frame  $R$  and  $[4.5]$  bands, using the best-fit SEDs in each bin. We find that toward redder  $R - [4.5]$  colors, the AGN contributes 89, 79, 29, and 12% at the  $R$  band and 74, 59, 43, and 60% at the  $[4.5]$  band. This suggests that the empirical  $R - [4.5]$  color is indeed a good proxy of AGN obscuration at optical wavelengths and that the QSO classification based on the  $R - [4.5]$  color is reliable. We then calculate

the average  $L_{\text{IR}}^{\text{SF}}$  ( $\langle L_{\text{IR}}^{\text{SF}} \rangle$ ) in bins of  $R - [4.5]$ . We again estimate the uncertainty in  $\langle L_{\text{IR}}^{\text{SF}} \rangle$  using bootstrap resampling.

We show the results in Figure 6(a). Even though the  $L_{\text{IR}}^{\text{SF}}$  difference between QSO1s and QSO2s is large,  $\langle L_{\text{IR}}^{\text{SF}} \rangle$  does not show the strong dependence on  $R - [4.5]$  seen for  $f_{250}$  and the average  $S_{250}$  (Figure 6(a)) within QSO1s and QSO2s. Additionally, the  $L_{\text{IR}}^{\text{SF}}$  differences between the far-IR-detected QSO1s and QSO2s and the far-IR nondetected QSO1s and QSO2s are only 0.14 and 0.17 dex, which are not as significant as the 0.30 dex difference between all QSO1s and QSO2s. Thus the higher  $\langle L_{\text{IR}}^{\text{SF}} \rangle$  of the QSO2 sample is mainly driven by its higher fraction of far-IR luminous SF galaxies.

### 5.2. $L_{\text{IR}}^{\text{SF}}$ versus $L_{\text{AGN}}$

To explore the connections between AGN and host galaxy growth rates in different QSO populations, we separately divide the QSO1s and QSO2s into bins of  $L_{\text{AGN}}$  and measure the  $\langle L_{\text{IR}}^{\text{SF}} \rangle$  for each bin. The uncertainties are again estimated by bootstrapping, as discussed in Section 5.1. We plot the  $L_{\text{AGN}} - L_{\text{IR}}^{\text{SF}}$  relations for QSO1s and QSO2s in Figure 6(b). We find that both the QSO1 sample and the QSO2 sample have a positive  $L_{\text{IR}}^{\text{SF}} - L_{\text{AGN}}$  correlation with similarly shallow slopes, with  $\log L_{\text{IR}}^{\text{SF}} \propto 0.25 \log L_{\text{AGN}}$  for QSO1s and  $\log L_{\text{IR}}^{\text{SF}} \propto 0.27 \log L_{\text{AGN}}$  for QSO2s. However, the  $\langle L_{\text{IR}}^{\text{SF}} \rangle$  for QSO2s is higher than that of QSO1s in each  $L_{\text{AGN}}$  bin by 0.28, 0.25, 0.32, and 0.28 dex.

For comparison, we also show the  $L_{\text{AGN}} - L_{\text{IR}}^{\text{SF}}$  model from Hickox et al. (2014), which assumes a direct, linear correlation between the average  $L_{\text{AGN}}$  and  $L_{\text{IR}}^{\text{SF}}$ , while the observed  $L_{\text{AGN}}$  is modulated by rapid variability. We calculate the Hickox et al. (2014) relation spanning the  $0.7 < z < 1.8$  redshift range in Figure 6 as the shaded region. We find that for all QSO2s besides those in the most luminous  $L_{\text{AGN}}$  bin, our result is consistent with the H14 model, and the QSO1s have  $L_{\text{IR}}^{\text{SF}}$  slightly lower than the model predictions throughout the entire  $L_{\text{AGN}}$  range. However, for both types of QSOs, the slope of the

$L_{\text{IR}}^{\text{SF}}-L_{\text{AGN}}$  relation appears to be shallower than the prediction of the simple model, if we take the different average redshift in each  $L_{\text{AGN}}$  bin into account.

As was shown by the results in Table 1, the average redshifts for more luminous QSOs are higher. Although our far-IR stacking approach can reliably measure the average far-IR fluxes and hence the average  $L_{\text{IR}}^{\text{SF}}$ , it is important to note that the difference in the average redshift between the lowest and the highest  $L_{\text{AGN}}$  bins is 0.5, and it is possible that the observed correlation between  $L_{\text{IR}}^{\text{SF}}$  and  $L_{\text{AGN}}$  is partially driven by the cosmic evolution of star formation and AGN accretion. Even though recent studies of the evolution of cosmic infrared luminosity density have shown that for the redshift range of the four  $L_{\text{AGN}}$  bins in Figure 6(b), the cosmic infrared luminosity is only weakly correlated with redshift ( $\rho_{\text{IR}} \propto (1+z)^{-0.3 \pm 0.1}$  for  $1.1 < z < 2.85$ , Gruppioni et al. 2013), there is still a substantial evolution in the specific SFR (SFR per unit stellar mass) of “main-sequence (MS)” SF galaxies (e.g., Elbaz et al. 2011).

A simple estimate of the effect of MS galaxy SFR redshift evolution can be made by calculating the average  $L_{\text{IR}}^{\text{SF}}$  for MS galaxies with  $M_{\star} = 10^{11} M_{\odot}$  at the redshift range of our QSO sample. From the theoretical framework of dark-matter halo-abundance matching methods (e.g., Behroozi et al. 2013),  $10^{11} M_{\odot}$  is the typical galaxy stellar mass hosted by dark-matter haloes of mass  $M_{\text{halo}} = 10^{13.1} [h^{-1} M_{\odot}]$ , which is the halo mass reported in recent clustering studies of mid-IR QSOs (e.g., Hickox et al. 2011; DiPompeo et al. 2014; Donoso et al. 2014). At the redshift of each QSO in our sample, the  $L_{\text{IR}}^{\text{SF}}$  for a  $10^{11} M_{\odot}$  MS galaxy can therefore be evaluated using the redshift-dependent SFR- $M_{\star}$  relation from Whitaker et al. (2012) and a Kennicutt relation,  $\text{SFR} = 1.09 \times L_{\text{IR}}^{\text{SF}}/L_{\odot}$  (Kennicutt 1998, modified for a Chabrier initial mass function). We find that the average  $L_{\text{IR}}^{\text{SF}}$  for MS galaxies evaluated using this approach is consistent with the average  $L_{\text{IR}}^{\text{SF}}$  in each  $L_{\text{AGN}}$  bin. This implies that for mid-IR quasars in this redshift range, the  $L_{\text{IR}}^{\text{SF}}$  and instantaneous  $L_{\text{AGN}}$  might not be directly connected but still follow similar redshift evolution. This suggests that a common physical parameter (e.g., a common gas supply) might be driving the evolution of both SMBHs and galaxies. This is also consistent with the recent study of Rosario et al. (2013), which showed that the  $L_{\text{IR}}^{\text{SF}}-L_{\text{AGN}}$  correlation for broad-emission-line QSOs is consistent with a scenario in which quasars are hosted by normal star-forming galaxies.

For mid-IR-selected AGNs, contamination from star-forming galaxy interlopers is also an issue that might introduce biases to the measurements of AGN and star formation luminosities. While our SED-fitting results show that 95% of the sources in our sample are indeed powerful QSOs with AGN-dominated mid-IR SED, it is still very important to verify that the observed  $L_{\text{IR}}^{\text{SF}}-L_{\text{AGN}}$  relation in Figure 6 is not caused by the incompleteness of our AGN selection criterion. In particular, a very powerful SF galaxy can harbor a heavily obscured AGN and still have starburst-like mid-IR SED. In such a case, the *IRAC* color of the SF galaxy would fall out of the Stern et al. (2005) selection wedge (e.g., Assef et al. 2010b; Kirkpatrick et al. 2012; Chung et al. 2014), and the sample selected with the Stern et al. (2005) wedge would show a biased  $L_{\text{IR}}^{\text{SF}}-L_{\text{AGN}}$  relation.

By happenstance, the mid-IR color of typical star-forming galaxy templates occupies the lower-left corner of the Stern et al. (2005) wedge at the redshift range of this sample (e.g., Donley et al. 2012, Figure 17). Therefore, any AGN contribution in addition to the SF galaxy templates would easily promote a SF galaxy into the AGN identification wedge. This is particularly true for our sample of luminous quasars. We test this effect by first normalizing the  $6 \mu\text{m}$  luminosity for AGN templates we used in the SED fitting described in Section 4 to  $L_{\text{AGN}} = 10^{45} \text{ erg s}^{-1}$  to meet the minimum  $L_{\text{AGN}}$  criterion of our QSO sample. We next combine these normalized AGN templates with two archetypical starburst galaxy templates, M82 and Arp 220, from Polletta et al. (2007). We find that to have a star-forming galaxy falling out of the AGN identification wedge while having an  $L_{\text{AGN}} \sim 10^{45} \text{ erg s}^{-1}$ , its  $L_{\text{IR}}^{\text{SF}}$  must exceed  $10^{47} \text{ erg s}^{-1}$ . This suggests that an SF galaxy must be a hyperluminous infrared galaxy (HyLIRG,  $L_{\text{IR}} > 10^{13} L_{\odot}$ ) to be able to hide an underlying quasar-like AGN component. According to the far-IR luminosity function of Gruppioni et al. (2013), there would only be less than two HyLIRGs in the redshift range of our sample given the size of the Boötes survey region. Because of the large number of sources in the lowest  $L_{\text{AGN}}$  bin of our sample, the inclusion of the two additional QSOs hidden in HyLIRGs would only affect the average  $L_{\text{IR}}^{\text{SF}}$  by 0.15 dex, which is still within the  $2\sigma$  range of the original  $L_{\text{SF}}$ .

We can also estimate biases in  $L_{\text{IR}}^{\text{SF}}$  due to the sources not selected in the AGN identification wedge by examining the SEDs of the sources not classified as mid-IR QSOs. In the redshift range of our sample, there are 77 SPIRE-detected sources outside the Stern et al. (2005) wedge. When we fit the SEDs of these sources we find that most of these powerful SF galaxies have no significant AGN contribution in the mid-IR. For the sources without a mid-IR AGN component, we assume that AGN contributes  $<10\%$  to the mid-IR monochromatic luminosity at  $6 \mu\text{m}$  as an upper limit. Only four of the 77 have  $L_{\text{AGN}}$  satisfying the  $L_{\text{AGN}} > 10^{45} \text{ erg s}^{-1}$  criterion. If we add these four sources into the lowest  $L_{\text{AGN}}$  bin, the average  $L_{\text{IR}}^{\text{SF}}$  would only increase by 0.05 dex. Therefore, we conclude that the  $L_{\text{SF}}-L_{\text{AGN}}$  correlation observed in Figure 6 is not biased by the exclusion of heavily obscured quasars hidden in powerful SF galaxies.

## 6. X-RAY PROPERTIES OF MID-IR QSOs

In Section 5, we have shown that for mid-IR-selected QSOs, the AGN obscuration at optical wavelengths and the AGN mid-IR luminosity can both be connected to the star formation of their host galaxies. Here we use an alternative AGN accretion rate indicator, the X-ray emission, to study the interplay between the far-IR-emitting dust and the X-ray emission.

We first count the number of detections in the far-IR and the X-ray observations. We note that the counts of X-ray detections can be affected by the varying sensitivity of the *Chandra* observations across the field (e.g., Mendez et al. 2013). However, the XBoötes observations are relatively uniform in depth ( $\sim 4 - 8 \times 10^{-15} \text{ erg s}^{-1}$ , Kenter et al. 2005), and this effect should be equivalent for both QSO types. The results of the detection fractions are summarized in Table 2. First, QSO1s have an X-ray detection fraction of 65%, which is much higher than the 12% far-IR detection fraction for QSO1s (see Section 3). For QSO2s, the X-ray detection fraction is only

**Table 2**  
Number of X-Ray-Detected Sources

	$N_X$	$N_{NX}$	$f_X$	$\langle z \rangle$	$\log \langle L_{6\mu m} \rangle (\text{erg s}^{-1})$	$\langle \log L_{\text{IR}}^{\text{SF}} \rangle (L_{\odot})$	$\langle L_X \rangle (\text{erg s}^{-1})$	$\langle A_V \rangle$
QSO1 (ALL)	356	190	0.65	1.24	46.20	11.74	$44.1 \pm 0.03$	0.32
QSO1 (FIR)	30	35	0.46	1.26	46.38	12.21	$43.9 \pm 0.09$	0.50
QSO1(No FIR)	326	155	0.67	1.24	46.17	11.62	$44.1 \pm 0.03$	0.28
QSO2 (ALL)	119	235	0.34	1.26	46.25	12.06	$43.7 \pm 0.05$	2.62
QSO2 (FIR)	23	74	0.24	1.24	46.27	12.34	$43.6 \pm 0.10$	2.85
QSO2(No FIR)	87	161	0.35	1.26	46.24	11.80	$43.8 \pm 0.05$	2.59

**Note.** The number counts and properties of different subsamples of QSOs classified based on the X-ray and far-IR detections. The properties listed here are the number of sources with X-ray detections ( $N_X$ ), the number of sources without X-ray detections ( $N_{NX}$ ), the X-ray detection fraction ( $f_X$ ), the average redshift ( $\langle z \rangle$ ), the average AGN bolometric luminosity ( $\langle \log L_{\text{AGN}} \rangle$ , see Section 3), the rest-frame 2–10 keV X-ray luminosity, and  $A_V$  (see Section 3 and Section 6).

34%, while the far-IR detection fraction is 27%. We also find that the presence of far-IR emission is associated with lower X-ray detection fractions in both QSO1s and QSO2s. For QSO1s, 91% of the X-ray-detected AGNs are not detected in the far-IR, while for QSO2s, 73% of the X-ray AGNs have no detectable far-IR emission. These number counts imply that large-scale dust might also play an important role in the absorption of X-rays.

Since a large fraction ( $\sim 76\%$ ) of the far-IR-detected QSO2s have no direct X-ray detection, these far-IR bright QSO2s might not be included in an X-ray-selected AGN sample. However, since both the far-IR and the X-ray observations in our sample are relatively shallow, the detection fractions only reflect the incidence of bright starburst and bright X-ray AGNs. To compensate for the shallow flux limit of the XBoötes survey, we use an X-ray stacking analysis to estimate the average X-ray luminosity for the sources without direct X-ray detections. We defined the stacked X-ray counts as the average number of background-subtracted photons detected within the 90% PSF energy encircled radius at 1.5 keV,  $r_{90}$ , where  $r_{90} = 1'' + 10''(\theta/10')^2$ . Here  $\theta$  is the off-axis angle from the *Chandra* optical axis.<sup>14</sup> We adopt 3.0 and 5.0 counts  $\text{s}^{-1} \text{deg}^{-2}$  for the diffuse X-ray background at the 0.5–2 and 2–7 keV bands, which closely matches the average background in annuli after excluding detected X-ray sources. We refer to Section 5.1.1 of H07 and Chen et al. (2013) for details about X-ray stacking analysis.

We performed the analysis on the subsamples listed in Table 2. To calculate the average X-ray luminosity for each subsample of QSOs, we first calculate the rest-frame 2–10 keV  $L_X$  for each X-ray-detected quasar from their observed 0.5–7 keV luminosity with a  $k$ -correction using the spectral index derived from the flux ratio between the soft (0.5–2 keV) and the hard (2–7 keV) bands. In detail, the X-ray spectrum was assumed to be a simple power law, and the hardness ratio was used to determine the power-law index ( $\Gamma$ ), using PIMMS and the ACIS Cycle 4 on-axis response function. For the X-ray-detected QSO1s, the average index is  $\Gamma = 1.83$ , which is typical for unabsorbed AGN X-ray spectra. For the X-ray-detected QSO2s, the average index of  $\Gamma = 1.24$  is consistent with AGNs with moderate absorbed spectra (Hickox et al. 2007). With the  $\Gamma$  derived from the observed hardness ratio, we  $k$ -corrected the observed-frame 0.5–7 keV luminosity to the rest-frame 2–10 keV, without deabsorbing the X-ray spectra. For the X-ray nondetected sources, we calculate their

average rest-frame 2–10 keV  $L_X$  by  $k$ -correcting the stacked 0.5–7 keV luminosity derived from the stacked X-ray flux, using the median redshift and the hardness ratio of stacked X-ray photons. The general X-ray properties of QSO1s and QSO2s have been discussed at length in Section 5 of Hickox et al. 2007. Combining the  $L_X$  of the individually X-ray-detected sources with the average  $L_X$  for the nondetected sources from stacking, we obtain the average X-ray luminosities in Table 2. These X-ray luminosities are the observed values and are not corrected for absorption. We also list the median extinction  $A_V$  of the AGN template at optical wavelengths from the SED-fitting results (see Section 4). For heavily obscured AGNs, the SED at optical wavelengths can be dominated by the host galaxy, and the average  $A_V$  may be a lower limit. However, we do find a much larger value of  $A_V$  for far-IR-detected QSO1s than that for far-IR nondetected QSO1s, which implies that the presence of star-forming dust attenuates both the optical and X-ray AGN emission.

We can also use the total numbers of stacked hard-band (2–7 keV) and soft-band (0.5–2 keV) photons to obtain the hardness ratio for different QSO subsamples. We find that for QSO1s, the HR remains a constant HR  $\sim -0.42$  for both the far-IR-detected and far-IR nondetected subsamples, while for QSO2s, the HR for both the far-IR-detected and far-IR nondetected subsamples are also very similar (HR  $\sim -0.12$ ). The large difference in the HR between QSO1s and QSO2s is consistent with the typical HR values for type I and type II X-ray AGNs, which has been demonstrated in H07. However, we here point out that the average hardness ratio is insensitive to the presence of far-IR-emitting dust. The uniform HRs for far-IR-detected and far-IR nondetected QSO2s might simply be due to the wide redshift distribution from which the stacked sources are drawn, since the uncertainties of the measured HRs correspond to more than 0.3 dex in  $N_{\text{H}}$  ( $2 - 5 \times 10^{22} \text{ cm}^{-2}$ , e.g., Figure 15 in H07) for the redshift range of our sample. However, the hardness ratios for the far-IR-detected and far-IR nondetected QSO1s are both consistent with little or no neutral gas absorption, which cannot explain the large  $L_X$  difference between far-IR QSO1s and far-IR nondetected QSO1s. Therefore, the constant HR, regardless of the presence of strong far-IR emissions, might imply that the lower average  $L_X$  and the higher  $A_V$  in far-IR-detected subsamples are due to gas of large column density that obscures X-ray photons in both the hard and soft bands. We note that large columns of ionized gas residing within 10 pc of the vicinity of the X-ray-emitting corona might also absorb both the hard-band and soft-band photons without altering the observed HR. As demonstrated in

<sup>14</sup> *Chandra* Proposer’s Observatory Guide (POG), available at <http://cxc.harvard.edu/proposer/POG>.

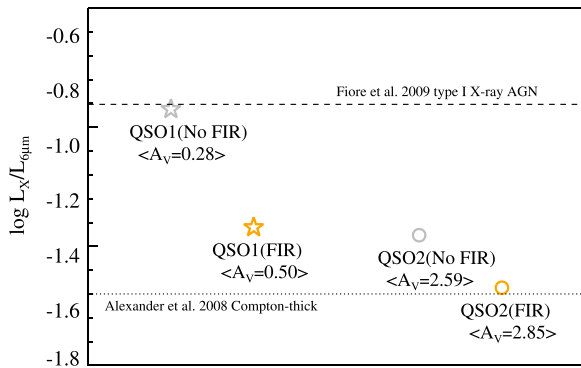


**Figure 7.** Summary of the  $L_X/L_{6\mu\text{m}}$  for different QSO populations. For comparison, we show the  $L_X/L_{6\mu\text{m}}$  relationship for type I X-ray AGNs using Equation 2 from Fiore et al. (2009) evaluated at  $L_{6\mu\text{m}} = 10^{44.9} \text{ erg s}^{-1}$  as the dashed line. We also show the  $L_X/L_{6\mu\text{m}}$  relation for local AGNs with Compton-thick obscurations (Alexander et al. 2008) as the dotted line. We show that the presence of far-IR-emitting dust attenuates the observed  $L_X$  in comparison to  $L_{6\mu\text{m}}$  and increases the AGN extinction in the optical wavelengths. We note that far-IR luminous QSO2s might not be detected in wide-field X-ray surveys due to the heavy obscuration that can be associated with the dust-enshrouded host galaxies.

various studies of X-ray spectral models (e.g., Ceballos & Barcons 1996), the observed hardness ratio is a much weaker function of the column density of the ionized warm absorber when compared to a neutral, cold absorber. This specific type of absorption has been observed in QSOs hosted by extremely luminous submillimeter galaxies (e.g., Page et al. 2011), similar to the luminous SF galaxies hosting QSO2s in this work. However, whether the same type of warm absorber exists in our far-IR-detected QSOs cannot be confirmed without high-resolution X-ray spectroscopy.

We summarize the results of our stacking analysis in Figure 7, where we show the ratio between  $L_{6\mu\text{m}}$  and  $\langle L_X \rangle$  for different subsamples of QSOs. Since  $L_X$  and  $L_{\text{MIR}}$  are both excellent tracers of SMBH accretion, and  $L_{\text{MIR}}$  is relatively insensitive to obscuration, the  $L_X$  to  $L_{\text{MIR}}$  ratio has been used to track down the elusive population of Compton-thick AGNs and to study the intrinsic AGN accretion rate (e.g., Lutz et al. 2004; Alexander et al. 2008; Gandhi et al. 2009; Eckart et al. 2010; Goulding et al. 2011b; Rovilos et al. 2013; Lansbury et al. 2014; Stern et al. 2014).

In Figure 7, we show that for both QSO1s and QSO2s, the existence of a far-IR detection is connected with smaller  $L_X/L_{6\mu\text{m}}$  ratios by at least 0.2 dex when compared to the far-IR nondetected subsamples. This indirectly supports a link between far-IR-emitting dust and the absorption of X-ray photons. For comparison, we also show the luminosity-dependent  $L_{6\mu\text{m}} - L_X$  relation by Fiore et al. (2009) evaluated at the average  $L_{6\mu\text{m}}$  of our sample  $L_{6\mu\text{m}} = 10^{44.9} \text{ erg s}^{-1}$ . We find that the  $L_X/L_{6\mu\text{m}}$  for QSO1s without direct far-IR detections is similar to the Fiore et al. (2009) relation. We note that for local active galaxies, an almost linear  $L_{6\mu\text{m}} - L_X$  relation has been reported by several studies (e.g., Lutz et al. 2004; Maiolino et al. 2007; Gandhi et al. 2009), but the inferred  $L_X/L_{6\mu\text{m}}$  value at  $L_{6\mu\text{m}} = 10^{44.9} \text{ erg s}^{-1}$  would be  $-0.37$  if we adopt Equation 2 from C.T.J. Gandhi et al. (2009), which is much higher than the results for our far-IR nondetected QSO1s and the Fiore et al. (2009) relation. The X-ray hardness ratio of the QSO1 sample is consistent with little or no X-ray absorption, suggesting that the different  $L_X/L_{6\mu\text{m}}$  ratios for QSOs and the X-ray-selected AGNs (Fiore

et al. 2009) observed are not simply due to the difference in gas absorption. The difference in the intrinsic mid-IR to X-ray spectral shape between local AGNs and quasars is beyond the scope of this work but will be addressed in a follow-up work by C. T. J. Chen et al. (2015, in preparation)

For AGNs with Compton-thick absorption, the observed  $L_X$  can be attenuated by a factor of more than 15 when compared to the intrinsic  $L_{6\mu\text{m}} - L_X$  relation (e.g., Alexander et al. 2008; Goulding et al. 2011a). We find that the  $L_X/L_{6\mu\text{m}}$  of our far-IR-detected QSO2s is consistent with the Alexander et al. (2008) relation derived from attenuating the X-ray luminosities for the  $L_X/L_{6\mu\text{m}}$  relation of local AGNs (Lutz et al. 2004) with Compton-thick material. However, recent observations have also discovered several luminous AGNs with extremely weak X-ray emissions even in the ultrahard energy bands probed by *NuSTAR* (Luo et al. 2013; Lansbury et al. 2014; Stern et al. 2014; Teng et al. 2014). Therefore, it is still unclear whether the low- $L_X/L_{6\mu\text{m}}$  ratio for the QSO2s is due to Compton-thick obscuration or intrinsic X-ray weakness. Nonetheless, the low  $L_X/L_{6\mu\text{m}}$  for far-IR-detected QSO2s is another line of evidence indicating that X-ray AGN selection methods can miss heavily obscured mid-IR QSOs hosted by galaxies with active SF activity. We caution that all AGN selection criteria suffer from various different selection biases, especially the incompleteness due to obscuration and the contamination from SF galaxy interlopers. We reiterate that SF galaxy contamination with our mid-IR color selection criteria is relatively mild for the shallow mid-IR flux limits of our sample. Our result demonstrates the advantage of mid-IR AGN selection criteria in detecting deeply obscured quasars hosted by powerful SF galaxies.

## 7. OBSCURED FRACTION AND $L_{\text{IR}}^{\text{SF}}$

In Sections 5 and 6 we have shown that mid-IR-selected QSO2s reside in galaxies with more active SF and that their AGNs are more obscured at both optical and X-ray wavelengths. While these results support the connection between AGN obscuration and star formation in the QSO host galaxies, we next directly test the connection between quasar obscuration and galaxy SF with the measurement of the “obscured fraction” as a function of  $L_{\text{IR}}^{\text{SF}}$ . We show this result in Figure 8. For the far-IR-detected QSOs, where  $L_{\text{IR}}^{\text{SF}}$  can be more accurately estimated, we separate the sources into two bins of  $L_{\text{IR}}^{\text{SF}}$  with an equal number of sources in each bin. For the QSOs with  $L_{\text{IR}}^{\text{SF}}$  estimated from stacked far-IR fluxes, the  $L_{\text{IR}}^{\text{SF}}$  suffer from larger uncertainties. Therefore, we do not group these QSOs based on their  $L_{\text{IR}}^{\text{SF}}$  but only evaluate obscured fractions for the entire populations. We find that the obscured fraction of the far-IR-detected QSOs is much higher than that of the rest of the QSOs, and the obscured fraction increases monotonically with respect to  $L_{\text{IR}}^{\text{SF}}$  as  $f_{\text{obs}} \propto 0.39 \times \log L_{\text{IR}}^{\text{SF}}$ . This agrees with a scenario which connects the obscuration in powerful quasars to the host galaxy star formation, as the AGN unification model does not predict an increased obscured fraction for QSOs hosted by galaxies with higher  $L_{\text{IR}}^{\text{SF}}$ .

## 8. VERIFICATION OF THE DIFFERENCE BETWEEN QSO1S AND QSO2S

In this work, we have demonstrated that the star formation properties of QSO1s and QSO2s are different, which implies a

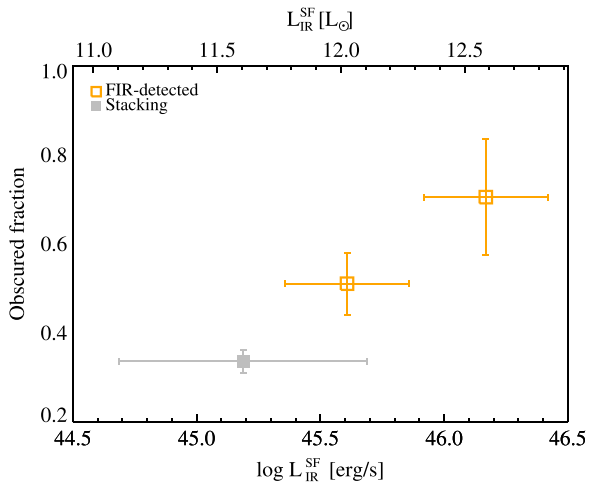


**Figure 8.** Obscured fraction (i.e., the QSO2 fraction) as a function of  $L_{\text{IR}}^{\text{SF}}$ . We separate far-IR-detected QSOs into two bins of  $L_{\text{IR}}^{\text{SF}}$  with an equal number of sources in each bin and plot their obscured fraction as the orange open squares. For the far-IR nondetected QSOs, we show the obscured fraction at the  $L_{\text{IR}}^{\text{SF}}$  estimated from stacking analysis as the gray filled squares. The horizontal error bars show the interpercentile range in  $L_{\text{IR}}^{\text{SF}}$  containing 80% of the sample. This plot shows a monotonic increase of obscured fraction at higher  $L_{\text{IR}}^{\text{SF}}$ , which connects the AGN obscuration to the host galaxy star formation.

link between star-forming dust and AGN obscuration in quasars. To verify the observed difference between QSO1s and QSO2 is not driven by the uncertainty of photometric redshifts of QSO2s and the presence of starburst contaminations, we perform several tests on the QSO1 sample and use the spectroscopically confirmed AGNs as a benchmark of how the various uncertainties might affect the observed properties of QSO2s.

### 8.1. Far-IR Detection Fraction

We reiterate that the sources with a dominating starburst component have been removed from the final sample studied in this analysis based on the SED fits discussed in Section 3. Therefore, the higher far-IR detection fraction for QSO2s is not due to the inclusion of starburst interlopers in the mid-IR AGN sample. Another possible issue that can drive the higher far-IR detection fraction for the QSO2s are the *photo-z* uncertainties. We here examine this issue by testing the null hypothesis that QSO1s and QSO2s have exactly the same far-IR detection fraction and redshift distribution.

From the AGES catalog, we select all of the sources with broad emission lines (the BLAGNs). In the AGES catalog there are a total of 1,619 BLAGNs, of which 181 of them have a SPIRE 250  $\mu\text{m}$  flux greater than 20 mJy. This far-IR detection fraction is similar to that for the QSO1 sample. To test if the uncertainties in photometric redshifts can boost the far-IR detection fraction, we randomly scatter the redshifts for all BLAGNs with the conservative uncertainty of  $\sigma_z = 0.25(1+z)$  (discussed in Section 2.1). In each random realization, we select the sources with a randomly assigned redshift within  $0.7 < z < 1.8$  and calculate their far-IR detection fraction. We repeat this process 100 times and find that on average, the random sample would have a far-IR detection fraction of only  $\sim 9\%$ . This means that the uncertainty in the photometric redshift would actually decrease the observed far-IR detection fraction if the far-IR luminosity function and the redshift distribution are the same for QSO1s and QSO2s. This is likely

due to the negative *k*-correction at 250  $\mu\text{m}$  for galaxies with typical cold-dust SEDs (e.g., Blain 1996; Negrello et al. 2007). The starburst cold-dust emission peaks at rest-frame  $\sim 100 \mu\text{m}$ , which corresponds to the SPIRE 250  $\mu\text{m}$  for an object at  $z = 1.5$ . Therefore, the starburst galaxies at lower redshifts are not brighter than our far-IR-detected QSOs at observed-frame 250  $\mu\text{m}$  due to the negative *k*-correction. High-redshift starbursts are also not likely to be included in our far-IR-detected sample, as the 250  $\mu\text{m}$  filter probes the rapidly dropping Rayleigh-Jeans tail of the cold-dust emission for objects beyond the redshift range of our sample.

Considering the significant difference of  $\sim 17\%$  between the far-IR detection fractions of QSO1s and QSO2s, we confirm that the QSO2s are indeed more likely to be hosted by galaxies with strong far-IR emission than QSO1s.

### 8.2. Far-IR Luminosity

Since the majority of QSO2s have only *photo-z*s, and luminosity measurements are redshift dependent, it is of extreme importance to confirm that the 0.3 dex average  $L_{\text{IR}}^{\text{SF}}$  difference between QSO1s and QSO2s is not driven solely by the uncertainty of *photo-z*s. Similar to the previous subsection, we estimate the effect of the *photo-z* uncertainty by testing the null hypothesis that the QSO2s have the same  $L_{\text{IR}}^{\text{SF}}$  distribution as the QSO1s. We again randomly assign redshifts to the AGES BLAGNs based on their *spec-z*s and the uncertainty upper limit  $\sigma_z = 0.25(1+z)$ . For the sources with a randomly assigned redshift within the  $0.7 < z < 1.8$  range, we perform the SED analysis (described in Section 3), using the assigned redshift, to calculate their average  $L_{\text{IR}}^{\text{SF}}$ . We repeat this process 100 times and find that the average  $L_{\text{IR}}^{\text{SF}}$  difference between the random samples and the original QSO1 sample is  $0.08 \pm 0.02$  dex, which is much smaller in comparison to the observed 0.3 dex difference between QSO1s and QSO2s. We also note that  $\sigma_z = 0.25(1+z)$  is a very conservative upper limit, so the effects of photometric redshift uncertainty are almost certainly smaller. The  $L_{\text{SF}}$  difference between QSO1s and QSO2s is not driven by the *photo-z* uncertainty.

## 9. DISCUSSION AND SUMMARY

Recently, a number of studies of X-ray-selected AGNs have found that star formation does not distinguish between AGNs with and without obscuration for AGNs classified based on either the presence of broad emission lines (Merloni et al. 2014) or the observed gas column density ( $N_{\text{H}}$ , e.g., Rosario et al. 2012; Rovilos et al. 2012). These conclusions are in direct contrast with our result in Figure 6 showing a significant ( $>0.25$  dex) difference in  $L_{\text{IR}}^{\text{SF}}$  between the QSO1s and the QSO2s.

To explain this apparent contradiction, we point out a fundamental difference between these studies and the present work. Merloni et al. (2014) classifies the X-ray-selected AGN into “type 1” and “type 2” sources based on SED fitting or the detection of broad emission lines. In our  $R - [4.5]$  classification, all of the QSO1s are spectroscopically selected type 1 quasars, but it is not clear how many of our QSO2s would have spectra with narrow emission lines similar to that of the optical type 2 quasars, since the large amount of dust which blocks most of the AGN optical continuum might very well block the emission lines from the narrow line region essential to optical AGN classifications. Also, while deep X-ray and optical observations

have proven to be efficient at detecting both obscured and unobscured AGNs, it is still challenging to include AGNs obscured by material with column density reaching  $N_{\text{H}} \sim 5 \times 10^{24} \text{ cm}^{-2}$  (i.e., Compton-thick) in optical or X-ray-selected samples. Recent works on synthetic models of the cosmic X-ray backgrounds (e.g., Gilli et al. 2007; Treister et al. 2009; Ballantyne et al. 2011) suggest that a significant fraction of SMBH growth might occur in a heavily obscured, rapidly accreting AGN phase. As we have shown in Figure 7, the far-IR-detected QSOs have a  $L_{\text{X}}/L_{6 \mu\text{m}}$  ratio consistent with AGNs that have heavily absorbed or intrinsically weak X-ray emission. Therefore, the different results might simply be due to mid-IR-selected quasars representing different AGN populations than the optically and X-ray-selected AGNs.

Indeed, mid-IR selection criteria have been shown to be capable of picking up sources with their nuclei obscured by Compton-thick material (e.g., Rovilos et al. 2013), and moderate-luminosity mid-IR AGNs have been found to preferentially populate the higher end of AGN Eddington ratio distributions (e.g., Hickox et al. 2009) and to reside in more blue, star-forming host galaxies (e.g., Hickox et al. 2009; Goulding et al. 2014). In conjunction with the higher  $L_{\text{IR}}^{\text{SF}}$  and obscuration in our mid-IR quasars, we argue that part of the enhancement in  $L_{\text{IR}}^{\text{SF}}$  of our sample when compared to X-ray or optical quasars is due to having different AGN populations based on different selection criteria and the heavy obscuration which possibly takes place on the scale of the host galaxy.

In summary, we have studied mid-IR luminous quasars at  $0.7 < z < 1.8$  and demonstrated a connection between obscuration in mid-IR-selected QSOs and star formation of their host galaxies. This connection is supported by the higher AGN obscured fraction in QSO host galaxies with larger  $L_{\text{IR}}^{\text{SF}}$  and the large differences in the average far-IR luminosities between QSO1s and QSO2s. We have also shown that both the AGN obscuration at optical wavelengths and the AGN absorption at X-ray wavelengths can be connected to the presence of far-IR-emitting dust. These results suggest that the large-scale gas and dust are also obscuring the central AGNs in addition to orientation-based small-scale obscuration, which is consistent with the scenario in which the rapidly growing SMBHs are connected to dust-enshrouded starburst galaxies.

We thank the anonymous referee for a careful reading of the manuscript and helpful suggestions that strengthened this paper greatly. We thank our colleagues on the AGES, ISS, SDWFS, NDWFS, and the XBoötes teams and the HerMES team for making the data publicly available. The first *Spitzer MIPS* survey of the Boötes region was obtained using GTO time provided by the *Spitzer* Infrared Spectrograph Team (PI, James Houck) and by M. Rieke. We thank the collaborators in that work for access to the  $24 \mu\text{m}$  catalog generated from those data by Emeric Le Floch. This work was supported under Contract NAS8-03060. R.J.A. was supported by Gemini-CONICYT Grant 32120009. K.N.H. and R.C.H. were partially supported by NASA through ADAP Award NNX12AE38G and by the National Science Foundation through Grant 1211096. This work was also supported by Science and Technologies Facilities Council (STFC) grant ST/I001573/1 (D.M.A. and A.D.M.) and the Leverhulme Trust (D.M.A.). R.C.H. acknowledges support from an Alfred P. Sloan Research Fellowship and Dartmouth Class of 1962 Faculty Fellowship. C.-T.J.C. was

supported by a Dartmouth Fellowship and the William H. Neukom 1964 Institute for Computational Science.

## REFERENCES

- Alberts, S., Pope, A., Brodwin, M., et al. 2013, *MNRAS*, 1, 2563  
 Alexander, D. M., Chary, R., Pope, A., et al. 2008, *ApJ*, 687, 835  
 Alexander, D. M., Bauer, F. E., Brandt, W. N., et al. 2011, *ApJ*, 738, 44  
 Antonucci, R. 1993, *ARA&A*, 31, 473  
 Ashby, M. L. N., Stern, D., Brodwin, M., et al. 2009, *ApJ*, 701, 428  
 Assef, R. J., Kochanek, C. S., Brodwin, M., et al. 2008, *ApJ*, 676, 286  
 Assef, R. J., Kochanek, C. S., Brodwin, M., et al. 2010a, *ApJ*, 713, 970  
 Assef, R. J., Kochanek, C. S., Ashby, M. L. N., et al. 2010b, *ApJ*, 722, 26  
 Assef, R. J., Kochanek, C. S., Ashby, M. L. N., et al. 2011, *ApJ*, 728, 56  
 Baldwin, J. A., Phillips, M. M., & Terlevich, R. 1981, *PASP*, 93, 5  
 Ballantyne, D. R., Draper, A. R., Madsen, K. K., Rigby, J. R., & Treister, E. 2011, *ApJ*, 736, 56  
 Behroozi, P. S., Wechsler, R. H., & Conroy, C. 2013, *ApJ*, 770, 57  
 Blain, A. W. 1996, *MNRAS*, 283, 1340  
 Brodwin, M., Brown, M. J. I., Ashby, M. L. N., et al. 2006, *ApJ*, 651, 791  
 Brown, M. J. I., Dey, A., Jannuzi, B. T., et al. 2007, *ApJ*, 654, 858  
 Brusa, M., Comastri, A., Gilli, R., et al. 2008, *ApJ*, 693, 36  
 Burlon, D., Ajello, M., Greiner, J., et al. 2011, *ApJ*, 728, 58  
 Canalizo, G., & Stockton, A. 2001, *ApJ*, 555, 719  
 Ceballos, M. T., & Barcons, X. 1996, *MNRAS*, 282, 493  
 Chapin, E. L., Chapman, S. C., Coppin, K. E., et al. 2011, *MNRAS*, 411, 505  
 Chary, R., & Elbaz, D. 2001, *ApJ*, 556, 562  
 Chen, C.-T. J., Hickox, R. C., Alberts, S., et al. 2013, *ApJ*, 773, 3  
 Chung, S. M., Kochanek, C. S., Assef, R., et al. 2014, *ApJ*, 790, 54  
 Dai, Y. S., Bergeron, J., Elvis, M., et al. 2012, *ApJ*, 753, 33  
 Dale, D. A., & Helou, G. 2002, *ApJ*, 576, 159  
 Del Moro, A., Alexander, D. M., Mullaney, J. R., et al. 2013, *A&A*, 549, A59  
 Di Matteo, T., Springel, V., & Hernquist, L. 2005, *Natur*, 433, 604  
 DiPompeo, M. A., Myers, A. D., Brotherton, M. S., Runnoe, J. C., & Green, R. F. 2014, *ApJ*, 787, 73  
 Donley, J. L., Rieke, G. H., Rigby, J. R., & Pérez-González, P. G. 2005, *ApJ*, 634, 169  
 Donley, J. L., Koekemoer, A. M., Brusa, M., et al. 2012, *ApJ*, 748, 142  
 Donoso, E., Yan, L., Stern, D., & Assef, R. J. 2014, *ApJ*, 789, 44  
 Draine, B. T. 2003, *ARA&A*, 41, 46  
 Drouart, G., De Breuck, C., Vernet, J., et al. 2014, *A&A*, 566, A53  
 Eckart, M. E., McGreer, I. D., Stern, D., Harrison, F. A., & Helfand, D. J. 2010, *ApJ*, 708, 584  
 Eisenhardt, P. R., Stern, D., Brodwin, M., et al. 2004, *ApJS*, 154, 48  
 Elbaz, D., Dickinson, M., Hwang, H. S. S., et al. 2011, *A&A*, 533, A119  
 Fiore, F., Puccetti, S., Brusa, M., et al. 2009, *ApJ*, 693, 447  
 Gandhi, P., Horst, H., Smette, A., et al. 2009, *A&A*, 502, 457  
 Georgantopoulos, I., Comastri, A., Vignali, C., et al. 2013, *A&A*, 555, A43  
 Gilli, R., Comastri, A., & Hasinger, G. 2007, *A&A*, 463, 79  
 Gonzalez, A. H., Brodwin, M., Brown, M. J. I., et al. 2010, *BAAS*, 216, 415.13  
 Goulding, A. D., & Alexander, D. M. 2009, *MNRAS*, 398, 1165  
 Goulding, A. D., Alexander, D. M., Mullaney, J. R., et al. 2011a, *MNRAS*, 411, 1231  
 Goulding, A. D., Alexander, D. M., Mullaney, J. R., et al. 2011b, *MNRAS*, 411, 1231  
 Goulding, A. D., Forman, W. R., Hickox, R. C., et al. 2014, *ApJ*, 783, 40  
 Griffin, M. J., Abergel, A., Abreu, A., et al. 2010, *A&A*, 518, L3  
 Griffith, R. L., & Stern, D. 2010, *AJ*, 140, 533  
 Gruppioni, C., Pozzi, F., Rodighiero, G., et al. 2013, *MNRAS*, 1, 32  
 Guainazzi, M., Matt, G., & Perola, G. C. 2005, *A&A*, 444, 119  
 Hainline, K. N., Hickox, R. C., Carroll, C. M., et al. 2014, *ApJ*, 795, 124  
 Harrison, C. M., Alexander, D. M., Mullaney, J. R., et al. 2012, *ApJL*, 760, L15  
 Harrison, F. A., Craig, W. W., Christensen, F. E., et al. 2013, *ApJ*, 770, 103  
 Hickox, R. C., Mullaney, J. R., Alexander, D. M., et al. 2014, *ApJ*, 782, 9  
 Hickox, R. C., Jones, C., Forman, W. R., et al. 2007, *ApJ*, 671, 1365  
 Hickox, R. C., Jones, C., Forman, W. R., et al. 2009, *ApJ*, 696, 891  
 Hickox, R. C., Myers, A. D., Brodwin, M., et al. 2011, *ApJ*, 731, 117  
 Hiner, K. D., Canalizo, G., Lacy, M., et al. 2009, *ApJ*, 706, 508  
 Hopkins, P. F., Hernquist, L., Cox, T. J., et al. 2006, *ApJS*, 163, 1  
 Jannuzi, B. T., & Dey, A. 1999, in ASP Conf. Ser. 191: Photometric Redshifts and the Detection of High Redshift Galaxies, ed. R. Weymann, L. Storrie-Lombardi, M. Sawicki, & R. Brunner (San Francisco, CA: ASP), 111  
 Kennicutt, R. C. 1998, *ARA&A*, 36, 189  
 Kenter, A., Murray, S. S., Forman, W. R., et al. 2005, *ApJS*, 161, 9

- Kirkpatrick, A., Pope, A., Alexander, D. M., et al. 2012, *ApJ*, 759, 139
- Kirkpatrick, A., Pope, A., Charmandaris, V., et al. 2013, *ApJ*, 763, 123
- Kochanek, C. S., Eisenstein, D. J., Cool, R. J., et al. 2012, *ApJS*, 200, 8
- Lacy, M., Petric, A. O., Sajina, A., et al. 2007a, *AJ*, 133, 186
- Lacy, M., Ridgway, S. E., Gates, E. L., et al. 2013, *ApJS*, 208, 24
- Lacy, M., Sajina, A., Petric, A. O., et al. 2007b, *ApJL*, 669, L61
- Lacy, M., Storrie-Lombardi, L. J., Sajina, A., et al. 2004, *ApJS*, 154, 166
- Lansbury, G. B., Alexander, D. M., Moro, A. D., et al. 2014, *ApJ*, 785, 17
- Luo, B., Brandt, W. N., Alexander, D. M., et al. 2013, *ApJ*, 772, 153
- Lutz, D., Maiolino, R., Spoon, H. W. W., & Moorwood, A. F. M. 2004, *A&A*, 418, 465
- Mainieri, V., Bongiorno, A., Merloni, A., et al. 2011, *A&A*, 535, A80
- Maiolino, R., Shemmer, O., Imanishi, M., et al. 2007, *A&A*, 468, 979
- Mateos, S., Alonso-Herrero, A., Carrera, F. J., et al. 2013, *MNRAS*, 434, 941
- Mendez, A. J., Coil, A. L., Aird, J., et al. 2013, *ApJ*, 770, 40
- Merloni, A., Bongiorno, A., Brusa, M., et al. 2014, *MNRAS*, 437, 3550
- Mullaney, J. R., Pannella, M., Daddi, E., et al. 2012, *MNRAS*, 419, 95
- Mullaney, J. R., Alexander, D. M., Goulding, A. D., & Hickox, R. C. C. 2011, *MNRAS*, 414, 1082
- Murray, S. S., Kenter, A., Forman, W. R., et al. 2005, *ApJS*, 161, 1
- Negrello, M., Perrotta, F., Gonzalez, J. G.-N., et al. 2007, *MNRAS*, 377, 1557
- Netzer, H. 2009, *MNRAS*, 399, 1907
- Netzer, H., Lutz, D., Schweitzer, M., et al. 2007, *ApJ*, 666, 806
- Oliver, S. J., Bock, J., Altieri, B., et al. 2012, *MNRAS*, 424, 1614
- Page, M. J., Carrera, F. J., Stevens, J. A., Ebrero, J., & Blustin, A. J. 2011, *MNRAS*, 416, 2792
- Page, M. J., Stevens, J. A., Ivison, R. J., & Carrera, F. J. 2004, *ApJ*, 611, L85
- Page, M. J., Symeonidis, M., Vieira, J. D., et al. 2012, *Natur*, 485, 213
- Park, S. Q., Barmby, P., Willner, S. P., et al. 2010, *ApJ*, 717, 1181
- Polletta, M., Tajer, M., Maraschi, L., et al. 2007, *ApJ*, 663, 81
- Polletta, M. D. C., Wilkes, B. J., Siana, B., et al. 2006, *ApJ*, 642, 673
- Rosario, D., Santini, P., Lutz, D., et al. 2012, *A&A*, 545, A45
- Rosario, D. J., Trakhtenbrot, B., Lutz, D., et al. 2013, *A&A*, 560, A72
- Rovilos, E., Comastri, A., Gilli, R., et al. 2012, *A&A*, 546, A58
- Rovilos, E., Georgantopoulos, I., Akylas, A., et al. 2013, *MNRAS*, 1, 2867
- Sanders, D. B., Soifer, B. T., Elias, J. H., et al. 1988, *ApJ*, 325, 74
- Sazonov, S., Willner, S. P., Goulding, A. D., et al. 2012, *ApJ*, 757, 181
- Schawinski, K., Simmons, B. D., Urry, C. M., Treister, E., & Glikman, E. 2012, *MNRAS*, 425, L61
- Serjeant, S., & Hatziminaoglou, E. 2009, *MNRAS*, 397, 265
- Shan, H. G., & Chen, P. S. 2012, *MNRAS*, 421, 235
- Silverman, J. D., Lamareille, F., Maier, C., et al. 2009, *ApJ*, 696, 396
- Somerville, R. S., Hopkins, P. F., Cox, T. J., Robertson, B. E., & Hernquist, L. 2008, *MNRAS*, 391, 481
- Stern, D., Eisenhardt, P., Gorjian, V., et al. 2005, *ApJ*, 631, 163
- Stern, D., Lansbury, G. B., Assef, R. J., et al. 2014, *ApJ*, 794, 102
- Sturm, E., Hasinger, G., Lehmann, I., et al. 2006, *ApJ*, 642, 81
- Sun, A.-L., Greene, J. E., Zakamska, N. L., & Nesvadba, N. P. H. 2014, *ApJ*, 790, 160
- Teng, S. H., Brandt, W. N., Harrison, F. A., et al. 2014, *ApJ*, 785, 19
- Treister, E., Urry, C. M., & Virani, S. 2009, *ApJ*, 696, 110
- Urry, C. M., & Padovani, P. 1995, *PASP*, 107, 803
- Usman, S. M., Murray, S. S., Hickox, R. C., & Brodwin, M. 2014, *ApJL*, 788, L3
- Whitaker, K. E., van Dokkum, P. G., Brammer, G., & Franx, M. 2012, *ApJL*, 754, L29
- Wilkes, B. J., Kuraszkiewicz, J., Haas, M., et al. 2013, *ApJ*, 773, 15
- Wright, E. L., Eisenhardt, P. R. M., Mainzer, A. K., et al. 2010, *AJ*, 140, 1868
- Zakamska, N. L., Gómez, L., Strauss, M. A., & Krolik, J. H. 2008, *AJ*, 136, 1607
- Zakamska, N. L., Strauss, M. A., Krolik, J. H., et al. 2006, *AJ*, 132, 1496